



Budapest University of Technology and Economics
Faculty of Electrical Engineering and Informatics
Department of Control Engineering and Information Technology

Geometric model and co-registration based approach for defining multiple patient diagnostic parameters

Scientific Students' Association Report

Author:

Sándor Bazsó, Dénes Fintha

Advisor:

Balázs Benyó, Ph.D.

Ákos Szlávecz, Ph.D.

Árpád Viola, M.D., Ph.D.

Angéla Hajdu, M.D

Contents

Kivonat	i
Abstract	ii
1 Introduction	1
1.1 Motivation	1
1.1.1 Clinical implication from orthopedic surgery	1
1.1.2 Respiratory system diagnostic	3
1.2 Goal of this research	3
1.3 Structure of the current report	3
2 Previous works	4
2.1 Methods of modelling and segmentation	4
2.2 Comparing our goals and methods with other works	5
3 Methods and Data	6
3.1 B-spline	6
3.2 Catmull-Rom spline	7
3.3 Curve for organ modelling	8
3.4 Closed B-spline fitting	8
3.5 Catmull-Rom spline fitting	8
3.6 Delaunay triangulation	9
3.7 Singular Value Decomposition	9
3.8 Analysed dataset	9
3.8.1 Spinal column validation dataset	11
3.8.2 Lung validation dataset	12
3.9 Validation metrics	13
3.10 Validation process	13
3.10.1 Spine model validation	14
3.10.2 Lung model validation	14

4	Results	16
4.1	Fitting process - manual part	17
4.1.1	Building blocks (2 nd step)	17
4.2	Fitting process - automatic part	19
4.2.1	Sorting the marked anatomical points (3 rd step)	19
4.2.2	B-spline fitting (4 th step)	19
4.2.3	Sorting and synchronisation of the layers (5 th step)	21
4.2.4	Catmull-Rom spline fitting and preliminary mesh calculation (6 th step)	23
4.2.5	Triangulation (7 th step)	24
4.2.5.1	Plate mesh	24
4.2.5.2	Surface mesh	25
4.3	Comparison	27
4.4	Diagnostic parameters	30
4.4.1	Angle measurement	30
4.4.2	Volume calculation	32
5	Discussion	33
5.1	Automatic fitting algorithms	33
5.1.1	Sorting the marked anatomical points	33
5.1.2	B-spline fitting	34
5.1.3	Sorting and synchronisation of the layers	34
5.1.4	Triangulation	35
5.1.5	Achieved precision of the model	36
6	Conclusions	39
6.1	Further work	40
	Acknowledgements	41
	Bibliography	42

Kivonat

Szervek szegmentációjára gyakran szükség van betegspecifikus diagnosztikai paraméterek meghatározása érdekében az orvoslás különböző területein, legyen az ortopédia, idegsebészet vagy pulmonológiai diagnosztika. A manuális szegmentáció általában pontos eredményt ad, azonban nagyon időigényes. Ennek alternatívája lehet képfeldolgozó eljárások alkalmazása a szegmentáció során, melyek azonban sok esetben pontatlan eredményt adnak, érzékenyek a különböző patológiás elváltozásokra, a megszokottól eltérő esetekre. Emiatt gyakran szükség van az így előállított modellek manuális korrekciójára, ami megint csak nehézkes és időigényes folyamat.

A jelen kutatás célja, egy gyors és robosztus szegmentációs módszer definiálása és implementálása, ami elegendően pontos ahhoz, hogy segítségével definiálhassunk betegspecifikus diagnosztikai paramétereket. A javasolt eljárás alapötlete egyszerű: a szegmentált szerv paraméterezett geometriai modelljét úgy állítjuk elő, hogy a modellparaméterek beállításával összeregisztráljuk azt a szerv háromdimenziós képével. Annak érdekében, hogy megvizsgáljuk a javasolt módszer alkalmazhatóságát és gyakorlati hasznát, olyan úgynevezett "modell-építőelemeket" definiáltunk, melyek egyszerű geometriai modellkomponensek és könnyedén használhatjuk őket különböző emberi szervek parametrikus modelljének összeállítására. Ezeket az építőelemeket használva több különböző emberi szerv (pl. gerincsigolya, tüdő, foggyökér) parametrikus modelljét állítottuk elő.

A TDK dolgozat bemutatja a javasolt módszert, a konkrét emberi szerveket leíró geometriai modelleket, a valós betegadatok alapján végrehajtott validáció lépéseit, valamint a modellek alkalmazását a konkrét diagnosztikai paraméterek meghatározása során.

Abstract

Organ segmentation as a part of the patient-specific diagnostic parameter definition is a typical prerequisite in several fields of medical diagnostics, such as orthopedics, neurosurgery, or pulmonary diagnostics. The manual segmentation provides a relatively accurate result, but the manual process is time-consuming. An alternative approach is using image processing methods to obtain the segmentation. However, these methods are often inaccurate and generally sensitive to pathological abnormalities or patient-specific deviations from the common cases. Thus, frequently manual correction of these models is necessary that is cumbersome again.

The overall goal of this research was to define and implement a quick and robust segmentation method that is accurate enough to allow organ segmentation based definition of patient-specific medical diagnostic parameters. The basic idea of the proposed segmentation method is simple: a parameterized geometric model of the segmented organ is defined that can be co-registered with the 3D image of the organ by adjusting the model parameters. To investigate the viability and practical benefits of the proposed approach, a set of so-called basic building blocks of geometric models are defined that could be used to easily build parametric models of different human organs. Using these building blocks parametric models of different human organs, such as vertebral body, lung, tooth canal, etc. are created and used to segment the corresponding human organ.

The research report introduces the proposed general concept, the concrete geometric models of human organs, the validation process using real patient data, and the application of the models for the definition of the human diagnostic parameters.

Chapter 1

Introduction

1.1 Motivation

In the last decade, medical imaging systems have greatly improved in respect of resolution and acquisition time, enabling them to be used for previously unimaginable purposes. This rapid improvement motivated the development of new image processing and analysis methods to extract the clinically relevant features and information from the medical images. One of the most frequently used feature extraction methods in medicine is the segmentation of individual organs. In fact, there are quite a few fields in the medical practice where organ segmentation can be used to improve the existing diagnostic methods and therapies and develop new ones. Below we introduce two fields of medicine from the vast amount of possible applications to demonstrate the importance of organ segmentation.

1.1.1 Clinical implication from orthopedic surgery

Orthopedic surgery treats the injuries, traumas and other conditions of the musculoskeletal system. This includes the fracture of bones, degenerative conditions of joints and tears of muscles and ligaments. After thorough discussion with neurosurgeons the following candidates as a possible application for the model were identified:

1. Calculation of the vertebral body's volume
 - Improvement of the PVP (Percutaneous Vertebroplasty) surgical intervention technique. This is a treatment procedure for collapsed vertebral bodies, more widely known as compression fracture. Mostly elderly people with osteoporosis suffer from this condition, where the underlying osteoporosis weakens the bone tissue, making it susceptible to fracture. Healthy individuals can suffer from this condition when being exposed to extreme trauma such as involvement in a car crash. One of the treatment option is the application of PVP, during which the vertebral bodies are filled with a cement like fixation agent, to stabilize them. This process could be improved by slightly modifying the circumstances of the surgical intervention process. One idea is by filling the vertebral body with saline solution before the injection of cement would allow a more homogeneous distribution of the fixation material (illustrated in Fig. 1.1). However it is difficult to measure quantitatively the achieved results due to the great variety in shape and size between the patients. This barrier can be mitigated by using a

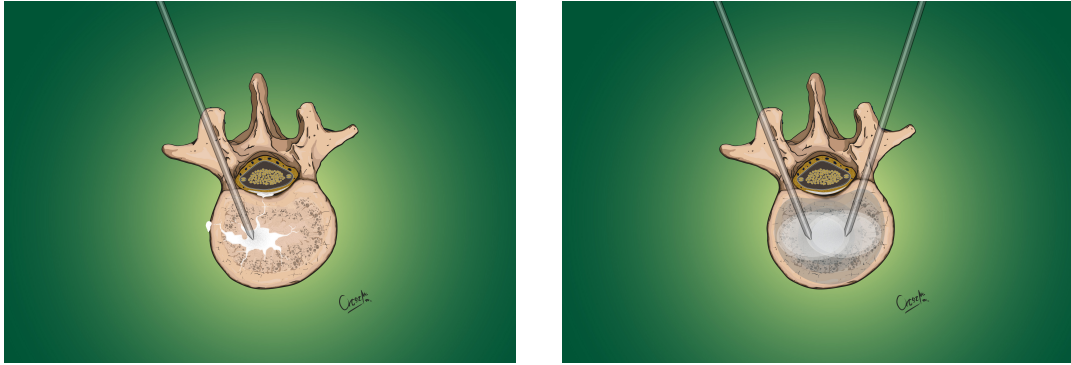


Figure 1.1: Illustration of percutaneous vertebroplasty surgical intervention using only cement (left) or cement and saline solution (right)

personalisable model of the individual patient's vertebra to calculate its volume and other key parameters.

- Studying the change in size and shape of the individual vertebral bodies with age.
2. Creation of a database with common angles (the angle measurement can be done using a geometrical model), that could be used as a reference when the angle of kyphosis or lordosis needs to be corrected.
 3. Determinating the shape and size of implants before surgery.
 4. Studying the spinal column's typical angle in the Caucasian race.

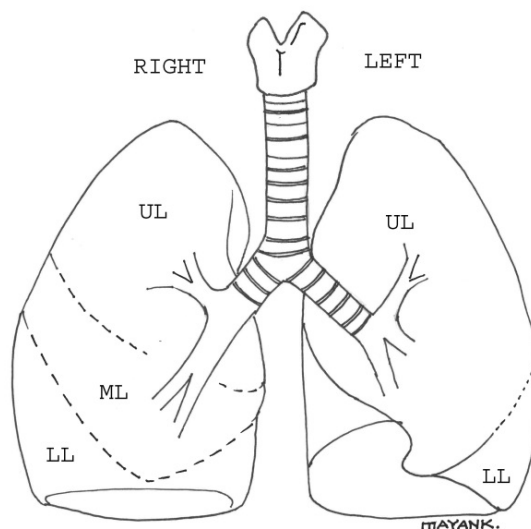


Figure 1.2: Two left and three right lobes of the lung [1][2]

1.1.2 Respiratory system diagnostic

One of the motivation for this research project came from the currently ongoing COVID-19 pandemic. In the clinical setup a key component in the evaluation of the patient's condition is by examining the pulmonary system. Generally it is done using a CT image of the lung. The radiologist evaluate the severity of the injury caused by the COVID-19 infection on the lung by giving a score from one to five to each lobe, based on his/her expertise, by looking at limited number of slices. However, this method is largely subjective due to heavily depending on the individual opinion of the medical professional when assigning these scores. Another major issue with this process is the failure to taking into account the size differences between the lobes (an example is shown in Fig. 1.2). A proper solution would be a quantitative evaluation of the lungs, where not only individual slices are accessed, rather the entire volume is analysed. One of the key requirement toward this evaluation system is a score on a linear scale. Such score would enable the medical experts to monitor the progression of the disease. In the future it could be integrated into a decision making system to help find the best treatment for an individual. To achieve this evaluation of the lungs as an initial step the segmentation of the lungs are necessary, which can be done using a geometrical model.

1.2 Goal of this research

Generalizing the above introduced two medical cases, the diagnostic parameter extraction frequently requires the segmentation of the organ subject of interest. Thus, we aim to develop a geometric model definition method of organs that allows the creation of patient-specific geometric models. The organ segmentation can be achieved by using this organ model which will be parametrized by co-registering the model with the 3D image of the patient's anatomy.

The geometric model is easy to fit the patient's individual anatomy, quick to define, but sufficiently precise. The model is created using reusable modelling building blocks, allowing the rapid development of new organ models. Several image processing and model optimisation steps are associated with the modelling building blocks enabling the semi-automated model fitting and image segmentation.

The created geometric models are suitable to define the diagnostic parameters required for medical decision-making directly. Thus, the proposed process is time efficient and precise, as proved in some preliminary medical studies.

1.3 Structure of the current report

The following chapter contains a brief overview of the articles and studies in the field of modelling and segmentation. The third chapter provides a detailed presentation of the mathematical tools and methods used for the definition of the geometrical model. In this chapter the analysed dataset and validation process with the evaluated metrics are presented too. The fourth chapter describes in details the developed geometrical model with the challenges needed to be resolved in the development of the model optimisation algorithms. The next chapter discusses the achieved results and analyses the model optimization algorithms, while pointing out some limitations. The final chapter provides a summary of the achieved results.

Chapter 2

Previous works

2.1 Methods of modelling and segmentation

The organ segmentation process marks the voxels of a 3D image belonging to a given organ. Organ segmentation methods of medical images are a topic of intensive research. It has plenty of applications in various fields of medicine, with each field having different goals to achieve. The availability of diagnostic parameters can significantly accelerate the diagnostics in fields like orthopedics [3] and pulmonology [4].

Most segmentation methods focus on the precise segmentation of a single organ or tissue, resulting in a three-dimensional organ model, typically represented by a set of voxels or as a triangular mesh. However, the more precise a segmentation is, the more manual intervention it requires, making the process time-consuming. As such, the speed of organ segmentation is a classic problem on which we could improve on.

The most traditional method of organ segmentation is marking the organ's voxel manually. Several image processing methods were developed to automate various phases of the manual image segmentation resulting in fully- or semi-automated image segmentation algorithms [5][6][7]. In the last couple of years, artificial intelligence (AI) methods found to be more efficient in medical image segmentation, and dozens of AI-based algorithms have been developed, generally on dedicated fields of medicine [8][9]. There have been successful attempts to segment muscle tissue [10], or even perform multi-organ segmentation [11] with this approach.

The result of these segmentation processes is still a set of voxels that can be visualized by a triangular mesh. Even though these methods could significantly reduce the segmentation time, the definition of diagnostic information requires additional processing steps.

An alternative approach of medical image segmentation is using the geometric model of the organ for the segmentation by adjusting the model parameters manually, so the geometric model will be registered to the organ. The prerequisite of this segmentation process is the organ model that can be easily registered to the organ's image.

Many organ models have been defined [12][13]. The primary goal of the definition of these models is the accurate description of the organ's geometry and defining a complex geometric shape as precisely fitting as possible to describe all the details of the segmented organ. Thus, these organ models typically use a large number of parameters. A typical example for such a model is the vertebral body model [14]) using 31 parameters to fit it to the organ accurately.

Applying these precise models in the organ segmentation process is almost impossible as the resulting segmentation method would be more time-consuming than the manual segmentation itself. This problem motivated our research, defining an appropriate geometric model easily applicable for organ segmentation.

2.2 Comparing our goals and methods with other works

Our main goal was reducing the time spent by the user segmenting organs, without losing a significant amount of precision in the process. As such, our modelling method has fewer parameters to set, while retaining as much precision as possible.

This is accomplished by defining a generic model of organs, which can be parametrized and reused. Parametrizing this model may yield various shapes (for example, a right lung, or a single vertebra [15][16]), and other, complex models can be built up as composites of such models (for example, a complete lung model consists of two lungs, and a spine model consists of multiple vertebrae).

Chapter 3

Methods and Data

Due to the methodological overlap with the scientific students' association report submitted in 2020, the method and data chapter's several subchapters are written based on the previously submitted report.

Curves are continuous lines in the space [17], typically described by a mathematical expression, where the solution of the expression defines the points of the curve in an n^{th} dimensional (usually 3D) space. In practical applications the curves are often defined with so-called control points associated with certain part of the curve and basis functions describing the exact path of the curve on the given segment. The points of the curve are calculated by incrementing the t input parameter of the basis function. We can use weights to define the control's scope of the control points. Applying t dependent weights of the control points we can ensure several continuity features of the curve. There are two types of basis functions:

- interpolating and
- approximating

basis function. The fundamental difference is whether the curve passes through each control points or just approach them. In the interpolating case there is a t_k value of t parameter for each control points where weight 1 is associated to the k control point and 0 to every other. In the approximating case there is no such condition.

The most simple type of curve is a polyline. The control points are connected with a continuous straight lines. It has sharp edges, which means it is not continuously differentiable. These type of curves are frequently referred to as C^0 .

Bézier curve is an approximating type curve, which only intersects the first and last control points. It is a C^2 type, which means it is a twice continuously differentiable curve. One disadvantage of the Bézier curve is its global control, meaning changing one control point changes the slope of the whole curve.

3.1 B-spline

B-spline is an approximating type of curve. The control points, knots and the degree of the spline unambiguously identifies it. The curve runs inside the convex shell of the polygon defined by the control points, which means the control points will determinate the path of the curve. A B-spline is a piecewise polynomial with a given degree. The parts are

separated with knots on the curve. In case of a first or higher degree B-spline the curve is approximated between neighbouring control points, therefore creating a continuous line. Increasing the degree of the spline will create a more smooth curve. A first degree B-spline will approximate with a straight line, a second degree will produce a continuously differentiable curve, while a third degree B-spline will create a twice continuously differentiable curve (see Figure 3.1). One of the advantage of B-spline is the local control over the curve, which means changing one control point will only modify the surrounding part of the curve while leaving the rest in place. Increasing the degree of the curve means that more control points take place in the definition of a single point on the curve. In practice it means that increasing the degree of the polynomial expression will lessen the local control. On the other hand moving two neighbouring knots toward each other will cause the curve to move closer to the specific control point, thus approximating it better.

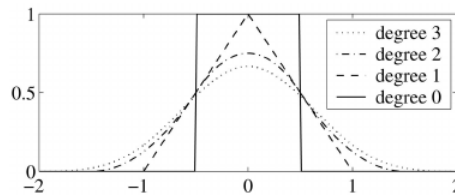


Figure 3.1: Degree of B-spline basis function from zero to three[18]

B-splines are widely used curves in different fields of industry. They can be used for drawing animated cartoon characters or rendering fonts. There is a broad spectrum of engineering applications too. From trajectory calculations for aircraft to modelling in the field of product design. Significant number of CAD (Computer Aided Design) software use B-spline for curved surfaces. The two major benefits over other curves are:

- smooth curve,
- local control.

Most of the organs has a smooth outline without sharp edges, thus making it suitable to track with a B-spline. The versatility of B-splines makes this type of spline a suitable candidate for organ modelling.

3.2 Catmull-Rom spline

In contrast with the B-spline, Catmull-Rom spline is an interpolating type curve. The tangent (v_k) in each control point is defined by the following expression:

$$v_k = \frac{p_{k+1} - p_{k-1}}{t_{k+1} - t_{k-1}}$$

where p_k is a control point and t_k is a knot. The Catmull-Rom spline is a piecewise third degree polynomial curve. It has a C^1 continuity, which means it's a continuously differentiable curve. When different derivatives are allowed at the two sides of a control point the continuity of the curve drops to C^0 . This construct provides a local control over the curve, meaning changing one control point only alters the surroundings of the given point.

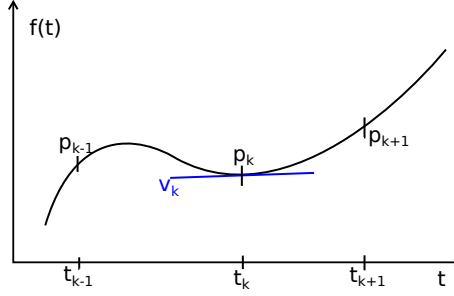


Figure 3.2: Catmull-Rom spline with tangent (v_k) at the p_k point

3.3 Curve for organ modelling

The organ modelling requires a closed curve, a loop to represent the outline of the given organ. This can be achieved differently with each type of spline. In order to create a closed curve from an open b-spline with $n + 1$ control points (P_0, P_1, \dots, P_n) and p degree another control point has to be added ($P_{n+1} = P_0$). Moreover $p + 2$ knots has to be added, which overlap with the first $p + 2$ knots ($u_{n+1} = u_0, u_{n+2} = u_1, \dots, u_{n+p+1} = u_p$). The closed curve's has C^{p-1} continuity at the joining point. A Catmull-Rom spline with $n + 1$ control points can be converted into a closed one, by adding a new control point the same way. If the two derivatives in this point equal the continuity of the curve will be C^1 .

Both Catmull-Rom and B-spline are suitable to model an organ's shape, the exact implementation could be decided in favour of one to another.

In order to visualize the model described with splines, a mesh has to be created. By evaluating the spline at point t the coordinate of that point can be acquired in 3D space. Incrementing t parameter with a predefined size will generate points on the curve. Joining these points with a straight line will provide a polyline representation of the original spline. By lowering the step size in the previous step a more accurate representation of the spline can be made.

3.4 Closed B-spline fitting

During the segmentation process the user marks key anatomical points on the 3D medical image along the perimeter of the organ. Then a B-spline curve is fitted on these points by finding the best solution for an overdetermined linear equation system. The result is a closed B-spline, specified by its control points and knots, that approximates the marked anatomical landmarks.

The most important parameter of this fitting algorithm is the number of desired control points. It determinates the constructed B-spline's ability to track complex shapes. Describing the B-spline with greater number of control points result in a curve that can follow elaborated anatomical structures.

3.5 Catmull-Rom spline fitting

In our application the Catmull-Rom spline have to be fitted on a given set of points. These points can be used directly as control points for the spline by taking advantage of the

interpolating property of the Catmull-Rom spline (Section 3.2 contains a brief description of this spline).

In contrast with B-spline the Catmull-Rom spline is specified only by its control points, no knots are involved in the determination of the curve's path. However an α parameter is used to control the overall shape of the curve. Based on the α value three type of Catmull-Rom splines can be distinguished:

- $\alpha = 0$: uniform,
- $\alpha = 0.5$: centripetal,
- $\alpha = 1$: chordal.

The α parameter can have an arbitrary value between 0 and 1, thus creating a curve that is a mixture of these types.

3.6 Delaunay triangulation

The geometric model is described by three-dimensional points originating from the selected segments and the smooth surface generated based on them. For three-dimensional imaging, and calculations, the model of the organ has to be triangulated.

Triangulation is done with the Delaunay triangulation method, which results in a triangular mesh that can be used in operations like exporting, and histogram calculation.

The Delaunay triangulation $DT(P)$ for a set P of points fulfills the criteria, that no point in P is inside the circumcircle of any triangles in $DT(P)$. A circumcircle is defined as a circle touching all the points of a given triangle.

This method results in a mesh consisting of non-overlapping triangles describing the surface of the segmented organ's model.

3.7 Singular Value Decomposition

Singular value decomposition is a mathematical method to factorize an $n \times k$ matrix \mathbf{M} , which represents a linear transformation from \mathbf{R}^k to \mathbf{R}^n , in the form of $\mathbf{M} = \mathbf{U} \cdot \mathbf{\Sigma} \cdot \mathbf{V}^*$.

- \mathbf{U} is an unitary $n \times n$ matrix, which represents the rotation in \mathbf{R}^n .
- $\mathbf{\Sigma}$ is an $n \times k$ diagonal matrix, which represents the coordinate scaling (to turn \mathbf{R}^k into \mathbf{R}^n).
- \mathbf{V} is an unitary $k \times k$ matrix, which represents the rotation in \mathbf{R}^k .

In our case, this method is used to fit planes and lines (see 4.2.3).

3.8 Analysed dataset

The two most frequently used medical imaging technologies that provide 3D anatomical structure of the human body are (see Figure 3.3)

- CT: Computer Tomography, and
- MRI: Magnetic Resonance Imaging.

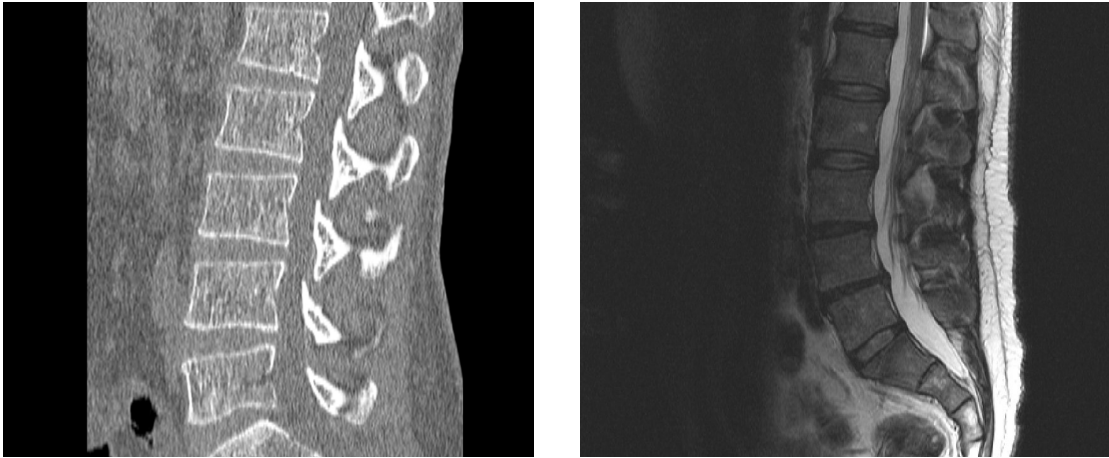


Figure 3.3: A sagittal slice of a CT (left) and MRI (right) showing a section of the spine
by gruntzooki is licenced under CC BY-SA 2.0[19]

There is a fundamental difference in the principals of CT and MRI imaging. CT machine calculates the voxel data from summational X-Ray images taken from different angles. Since X-Rays are attenuated more by dense tissues, for example bones than by soft tissue, this modality displays the skeleton with better contrast than it shows the internal organs. To standardize the CT images, a quantitative scale was introduced, called Hounsfield scale. Certain tissues are represented with a specific Hounsfield unit as shown on Figure 3.4. In this way unifying images of different vendor's machine and simplifying the interpretation of the data. On the other hand the MRI machine measures magnetic resonance. The human body is largely composed of water molecules. In each molecule there are two hydrogen atoms. MRI excites the hydrogen atoms with a large magnetic field and measures the radiation emitted by these excited atoms. Therefore it creates with higher contrast image where water is present in higher concentration. In practice this means the MRI creates a more detailed image of the soft tissue, and the skeleton is not visible. Both images can be enhanced with the use of contrast material to highlight parts relevant for the examination.

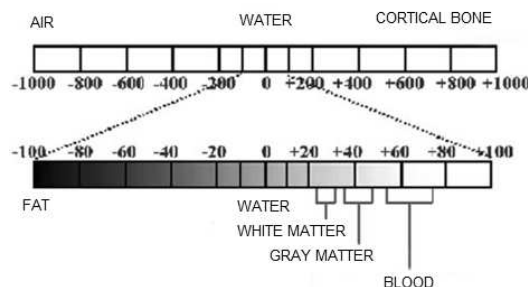


Figure 3.4: Hounsfield scale from -1000 to 1000 highlighting the typical values of different tissues [20]

3.8.1 Spinal column validation dataset

To validate our model we selected the lumbar segment of the vertebral column. The vertebrae of this part of the spine shows greater consistency in size and shape compared to the cervical section. Thoracic part would have meet this criteria as well but it has 12 vertebrae compared to the 5 of the lumbar section, that would have required more labour work to fit the model. CT is preferred over MRI, as it provides richer contrast when displaying bones. The third requirement toward the dataset: an available mask for the vertebrae to use as ground truth in the validation process.

We used a segmented lumbar vertebra CT database from the *University of Ljubljana, Faculty of Electrical Engineering, Laboratory of Imaging Technologies* [21][22]. This database contains 10 CT image of patients' lumbar section of the vertebral column, with each vertebra hand segmented in it. This database was selected because it fulfils the above-mentioned three requirements (CT image, lumbar section, available mask).

Table 3.1 shows the technical parameters of the images in the database. Spacing shows the voxels' distance from each other, while the resolution gives the number of voxels in each dimension.

The database contains 7 male and 3 female subject's CT image, with mean age of 46 years, and 13.5 years standard deviation. 4 out of 10 patients has a healthy lumbar spine, we selected those for the modelling and analysis.

Image	Spac. S [mm]	Spac. C [mm]	Spac. A [mm]	Res. S	Res. C	Res. A
Subject01	0.28	0.28	1.07	1024	1024	200
Subject02	0.33	0.33	0.91	1024	1024	219
Subject03	0.34	0.34	0.81	1024	1024	260
Subject04	0.33	0.33	1.00	1024	1024	200
Subject05	0.37	0.37	1.28	1024	1024	200
Subject06	0.41	0.41	1.53	1024	1024	200
Subject07	0.33	0.33	0.97	1024	1024	240
Subject08	0.49	0.49	1.00	1024	1024	218
Subject09	0.45	0.45	1.13	1024	1024	270
Subject10	0.79	0.79	0.73	512	512	323

Table 3.1: Image technical parameters in the vertebra database
(S - Sagittal, C - Coronal, A -Axial)

The images and the mask of the individual vertebrae are stored in a so called nearly raw raster data format (*.nrrd). This file format has two parts. A header where the most necessary metadata of the image is stored (spacing of the voxel, resolution, etc.), and a data section which can be compressed.

The modelling framework used in this study only supports DICOM (Digital Imaging and Communications in Medicine) format. This file type is developed for storing and transmitting medical images. Nowadays most of the scanners, workstations and visualisation software support this format. It has a rich metadata header which stores detailed information about the image, scanner, patient and the type of the examination. It has a wide range of supported modalities from radiography, ultrasonography, CT, and MRI.

In order to load the *.nrrd format images into the framework they need to be converted into DICOM format. The conversation was done in 3D Slicer, which is an open source flexible and modular platform for medical image processing and analysis. It has a rich toolset for

handling various image formats, advanced visualization features, segmentation and more. 3D Slicer were used for converting the images from *.nrrd format to DICOM and applying a transformation. Later was necessary to rotate the image into the traditional orientation, where the top of the axial view shows the anterior of the patient, the left side corresponds to the right side of the patient. In coronal view the head is towards the top of image, and the patient’s left side is on the right. In sagittal view the head is towards the top of the image and the left side of it correspond to the anterior direction (see Figure 3.5). Finally, an offset had to be applied on the data to represent a Hounsfield scale.

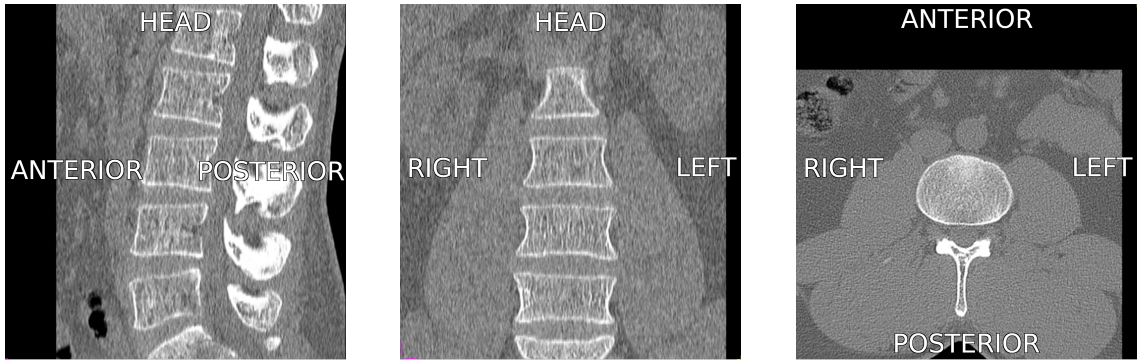


Figure 3.5: CT directions: Sagittal (left), Coronal (middle), Axial (right)

3.8.2 Lung validation dataset

The key expectation toward the database: a 3D medical image with segmentation mask of the lungs. This requirement were fulfilled by the *2017 Lung CT Segmentation Challenge* database [23][24][25], which contains lung CT images of 60 patients. The image acquisition was done in 3 different institutes. The images in this dataset are either 4DCT or free-breathing (FB) CTs. The 4DCT means multiple images are captured in the breathing cycle thus allowing a video like replay of the chest movements during breathing. A manual segmentation of the lungs, oesophagus, heart and spinal cord is available for the database stored in DICOM RTSTRUCT format.

5 patients’ records were selected for validation from this database. The most important technical parameters of these images are summarized in Table 3.2.

Image	Spac. S	Spac. C	Spac. A	Res. S	Res. C	Res. A
LCTSC-S1-101	0.98	0.98	3.00	512	512	130
LCTSC-S1-102	0.98	0.98	3.00	512	512	148
LCTSC-S1-201	0.98	0.98	3.00	512	512	117
LCTSC-S2-101	0.98	0.98	2.50	512	512	160
LCTSC-S2-102	0.98	0.98	2.50	512	512	176

Table 3.2: Image technical parameters in the lung database
Spacing in mm (S - Sagittal, C - Coronal, A -Axial)

3.9 Validation metrics

In order to quantify the precision of the model similarity metrics were evaluated. These metrics give a numerical value representing the accuracy of the model based on given aspects.

Hausdorff metric is commonly called Hausdorff distance as its output can be interpreted as some sort of distance between the two compared sets. We evaluated the following 3 metrics related to Hausdorff distance:

- Hausdorff maximum distance ($d_H(X, Y)$): The maximum distance for all points in X, to the closest point in Y and vice versa. Formal mathematical expression:

$$d_H(X, Y) = \max \left\{ \max_{x \in X} \min_{y \in Y} d(x, y), \max_{y \in Y} \min_{x \in X} d(x, y) \right\} \quad (3.1)$$

- Hausdorff average distance ($d_{H,avg}(X, Y)$): The average distance for all points in X, to the closest point in Y and vice versa. Formal mathematical expression:

$$d_{H,avg}(X, Y) = \frac{1}{2} \cdot \left(\frac{1}{|X|} \sum_{x \in X} \min_{y \in Y} d(x, y) + \frac{1}{|Y|} \sum_{y \in Y} \min_{x \in X} d(x, y) \right) \quad (3.2)$$

- 95% Hausdorff distance: Similar to maximum Hausdorff distance, but the top 5% discarded, thus eliminating any error from a small set of outliers.

Dice coefficient is another typical metric for evaluating two sets similarity. 5 metrics were calculated:

1. Dice coefficient: Measures the overlap between the two sets (X and Y). Can be calculated with the following formula:

$$Dice = \frac{2|X \cap Y|}{|X| + |Y|} \quad (3.3)$$

where \cap represents the intersection and $+$ represents the union.

2. True positive (%): In the model the given voxel is correctly part of the organ.
3. True negative (%): In the model the given voxel is correctly not part of the organ.
4. False positive (%): In the model the given voxel is incorrectly marked as part of the organ.
5. False negative (%): In the model the given voxel is incorrectly marked as not part of the organ.

3.10 Validation process

In order to validate our model we compared the result with a ground truth. The later was obtained together with the dataset in the form of a hand made segmentation of the organ. These reference masks are available as a voxel array, therefore, to compare the final model with a reference, the model has to be voxelized. The algorithm's inputs are the desired

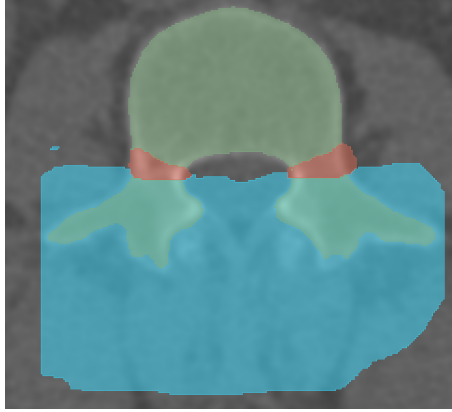


Figure 3.6: Cropping of the reference; green: reference mask, blue: *processes of the vertebra to remove*; red: *pedicle of vertebral arch* (this area is not checked).

resolution and spacing of the voxel array, which parameters are identical with the medical image parameters, and the triangular mesh representing the model. Each voxel of the 3D medical image is categorised based on whether the centre of the voxel is located inside or outside the model’s closed surface. The output is generated in the previously introduced *.nrrd format.

The comparison was done with 3D Slicer. First the reference and exported voxel arrays are loaded into the program as label maps. After that various similarity metrics are calculated between the reference and the model using SlicerRT [26] extension of the 3D Slicer.

3.10.1 Spine model validation

The selected dataset provides a hand made segmentation, but the mask contains the entire vertebra, while we only modelled the vertebral body. To be able to properly validate the model we had to crop the reference mask. In the first step the *processes of the vertebra* were removed from the reference (marked with blue colour in Fig. 3.6). In addition it is hard to determinate the exact boundary of the *vertebral body* where it joins to the pedicle of the *vertebral arch*. To overcome this issue an area was defined around the connection point of the *vertebral body* and the *pedicle of vertebral arch* which area was excluded from the comparison between the reference and the model (marked with red colour in Fig. 3.6). This area was carefully defined to minimize its size in order to reduce it’s effect on the validation result and in order to retain as much as possible from the region next to the *foramen vertebrale*, since this part of the model is critical in a medical application. The exclusion from the comparison was achieved by removing this domain from the reference and model too, thus making a perfect fit in this section.

3.10.2 Lung model validation

The validation of the lung model were done using the available reference mask (an example is shown in Fig. 3.7) A comparison between the mask and the model were performed by evaluating Hausdorff distance and Dice coefficient.

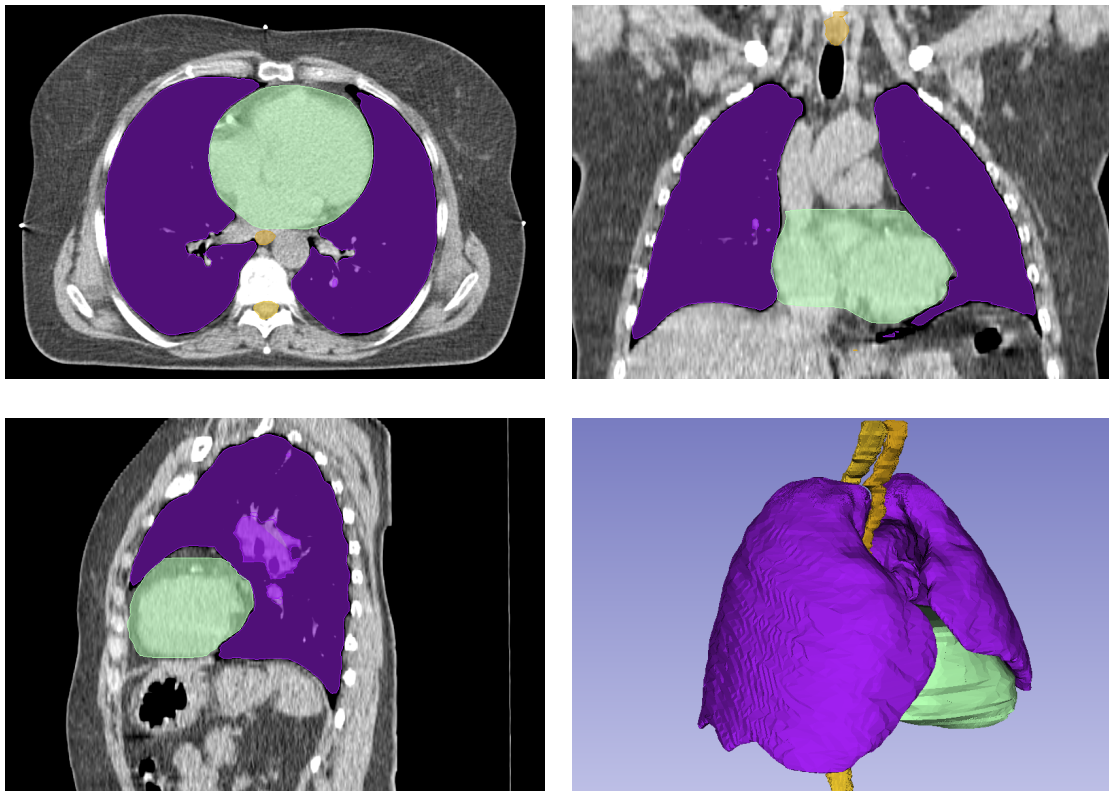


Figure 3.7: Reference mask for the lung model. Top left: axial, top right: coronal, bottom left: sagittal, bottom right: 3D view. Purple: lungs, green: heart, yellow: oesophagus and spinal cord

Chapter 4

Results

The proposed geometric model construction is built on anatomical landmark definition. Identifying anatomical landmarks in medical diagnostics is a common practice and used in the daily routine of medical experts. Using these anatomical landmarks to define the geometric model of the organs is a logical, straightforward extension of the diagnostic process. This approach allows us to optimise the geometrical model for the segmentation process, by making it easy and time-efficient to co-register the model with the patient's 3D image. A typical example for a geometric model of a human organ is shown in Fig. 4.1 where we can see a vertebral body model. The surface of the model is defined by mathematical curves. In this example, B-splines form the outline of the given organ in horizontal planes (marked with green colour in Fig. 4.1), while Catmull-Rom splines describe the surface of the given organ (marked with blue colour in Fig. 4.1). Altogether, the vertebral body model in Fig. 4.1 consists of three horizontal planes (3 B-splines) and 32 Catmull-Rom splines.

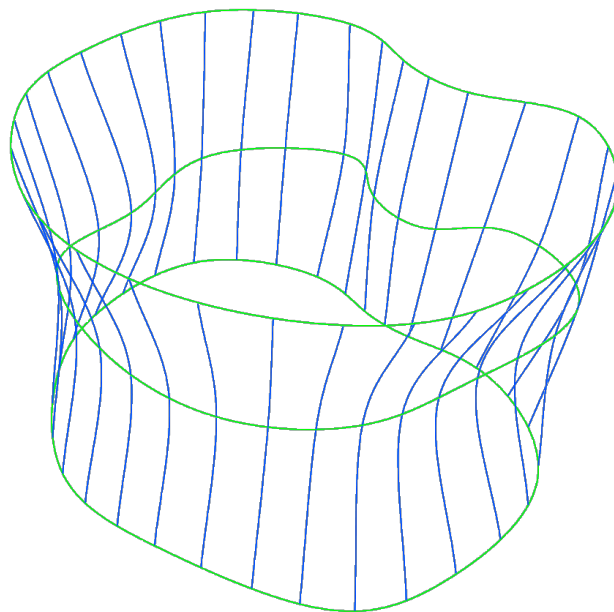


Figure 4.1: Geometrical model's structure (vertebral body)
Splines: green: B-spline; blue: Catmull-Rom spline

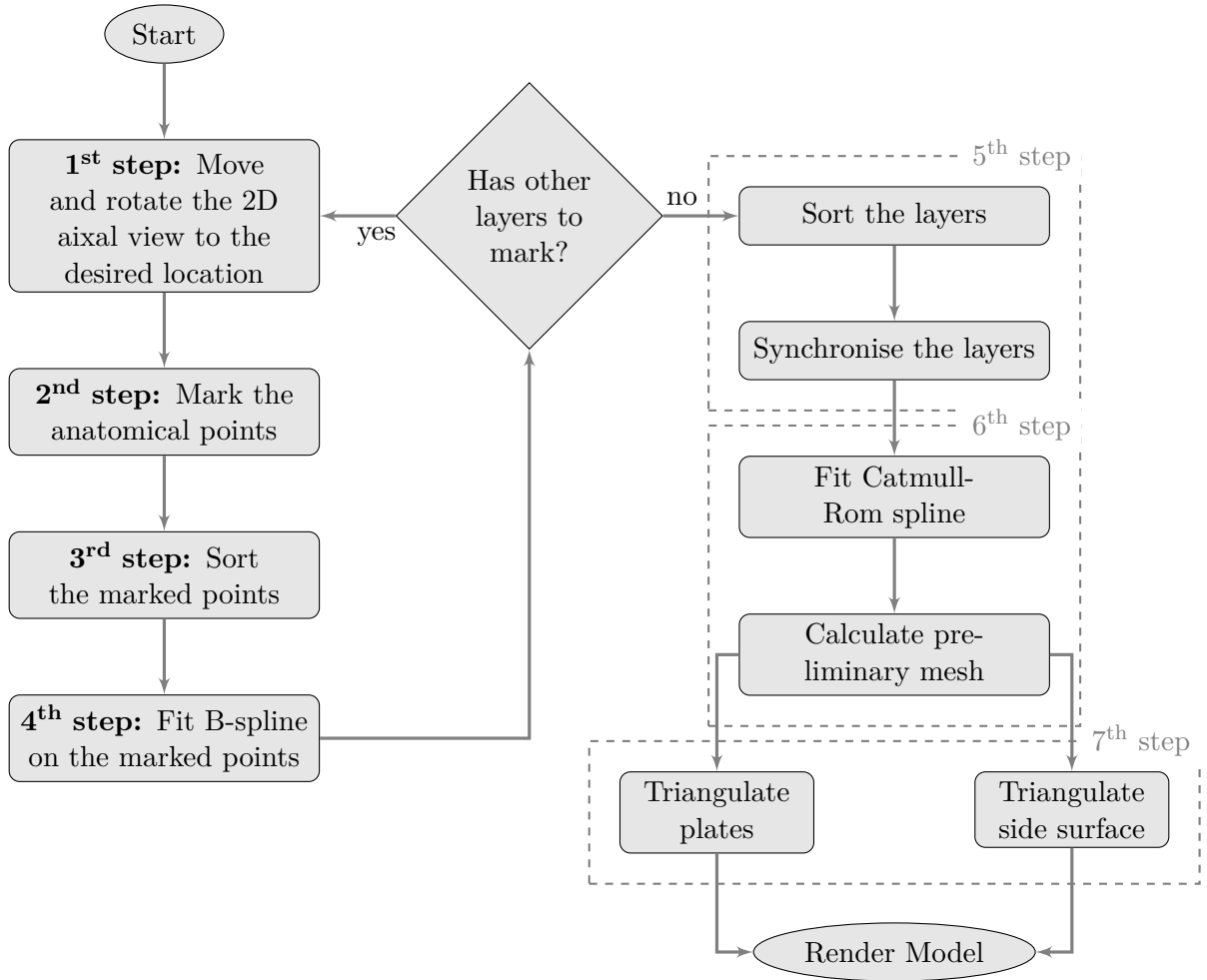


Figure 4.2: Workflow of the model fitting

4.1 Fitting process - manual part

The workflow of the model fitting process is presented in Fig. 4.2. The first two steps require manual input from the medical professional, while the rest is automatically executed. After loading the 3D medical image (CT or MRI), the user moves and rotates it to line up the axial view with the desired plane of the anatomical structure being modelled.

To model a vertebral body, based on our consultations with neurosurgeons, we have chosen to build the model from 3 planes. The vertebral body's 2 base plates and a third one in-between them (as shown in Fig. 4.3).

Other organs, that have more features on their surface, such as lungs, may require more planes, to accurately track the outline of the organ. The model is constructed to allow later refinement. This is achieved by adding more layers at critical points.

4.1.1 Building blocks (2nd step)

In the second step (see Fig. 4.2) the medical professional marks the outline of the organ. To achieve this there are several building blocks available for the user:

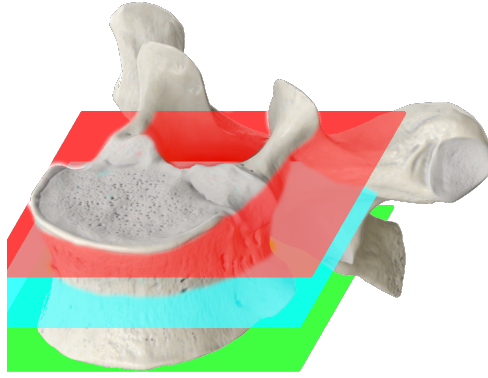


Figure 4.3: 3 planes of the vertebral body modelling

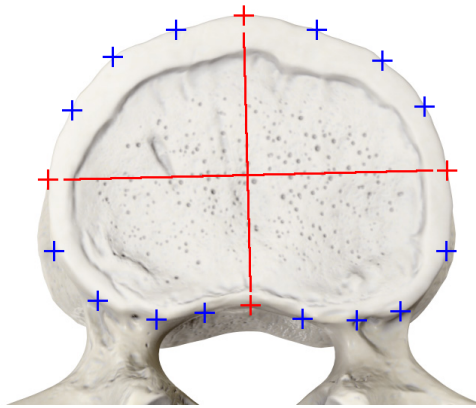


Figure 4.4: Marked anatomical points on the outline of the vertebral body. Red: important points, Blue: ordinary points

- A) Simple curve representing the outline of the given organ defined by equally important marker points.
- B) Simple curve representing the outline of the given organ defined by important and non-important marker points. (Important markers are approximated with significantly less error when the B-spline curve is fitted.)
- C) Two curves for the modelling of hollow structures. One represents the outer contour and one the inner contour of the organ. The two curves could be any type of the above mentioned ones.

In the vertebral body modelling workflow we opted to use simple curves with important and non-important markers. We decided to use important markers on the axis of the vertebral body's base plate. This is shown in Fig. 4.4, where the 4 red markers are important points, while the blue ones are ordinary markers.

When modelling lungs it is necessary to use a combination of the building blocks. The superior part of the lung can be represented with a simple curve, but the inferior section do to the protrusion of the diaphragm has a concave shape. Closely examining this geometrical configuration, we concluded that it has the properties of a hollow structure,

because in some slices the lung tissue surrounds the diaphragm. Therefore, it is required to use an outer and inner curve to precisely describe the model.

4.2 Fitting process - automatic part

The subsequent processing steps after step 2 are executed automatically. The purpose of these actions are to create a precise geometrical model with as few as possible marked anatomical points. Another benefit would be the reduction of the required user interaction thus accelerating the whole model fitting process.

4.2.1 Sorting the marked anatomical points (3rd step)

In each layer the marked anatomical points have to be sorted according to the desired order. This step is necessary because the modelling framework allows the user to mark the anatomical points in an arbitrary order. This provides greater flexibility when the model fitting is done, since it is possible to insert a marker later to refine the model.

Fig. 4.5 presents the steps of the landmark sorting algorithm. This is a distance based ordering method. In an initialization step distances between each landmarks are calculated. Then a starting marker is selected. From there always the closest non-visited marker is added to the chain until no markers left. After the last marker is processed the chain is closed by adding the first marker as the final element. Then the entire length of the loop is calculated. This value is used later for optimisation purposes.

The above described algorithm yield different result based on the starting point. Therefore the calculation is done multiple times, each time selecting a different landmark as the starting point. After that the best configuration chosen based on the length of the loop.

The subsequent processing steps require consistent ordering of the landmarks, meaning all loops have to have a clockwise direction. It is achieved by checking the direction of the loop and reversing it in the final step if necessary.

4.2.2 B-spline fitting (4th step)

In this step a closed B-spline (introduced in Section 3.1) is fitted on the given landmarks. The fitted spline is a 3rd degree B-spline. The algorithm were designed to support the building blocks presented in Section 4.1.1. This is achieved by distinguishing so-called important and non-important landmarks. The significant ones are approximated by the B-spline with significantly less error than the ordinary ones.

This process provides different result based on the starting landmark. This feature of the B-spline fitting algorithm is not desired, therefore it is mitigated by iterating over all landmarks. A maximum deviation from the predefined landmarks are calculated with each starting point, then the best configuration is selected.

It is important to properly select the number of control points for the B-spline to model the given organ precisely. Supposing too few control points the B-spline will be unable to model complex structures. With more than the necessary number of control points, the spline would have an undesired wiggle.

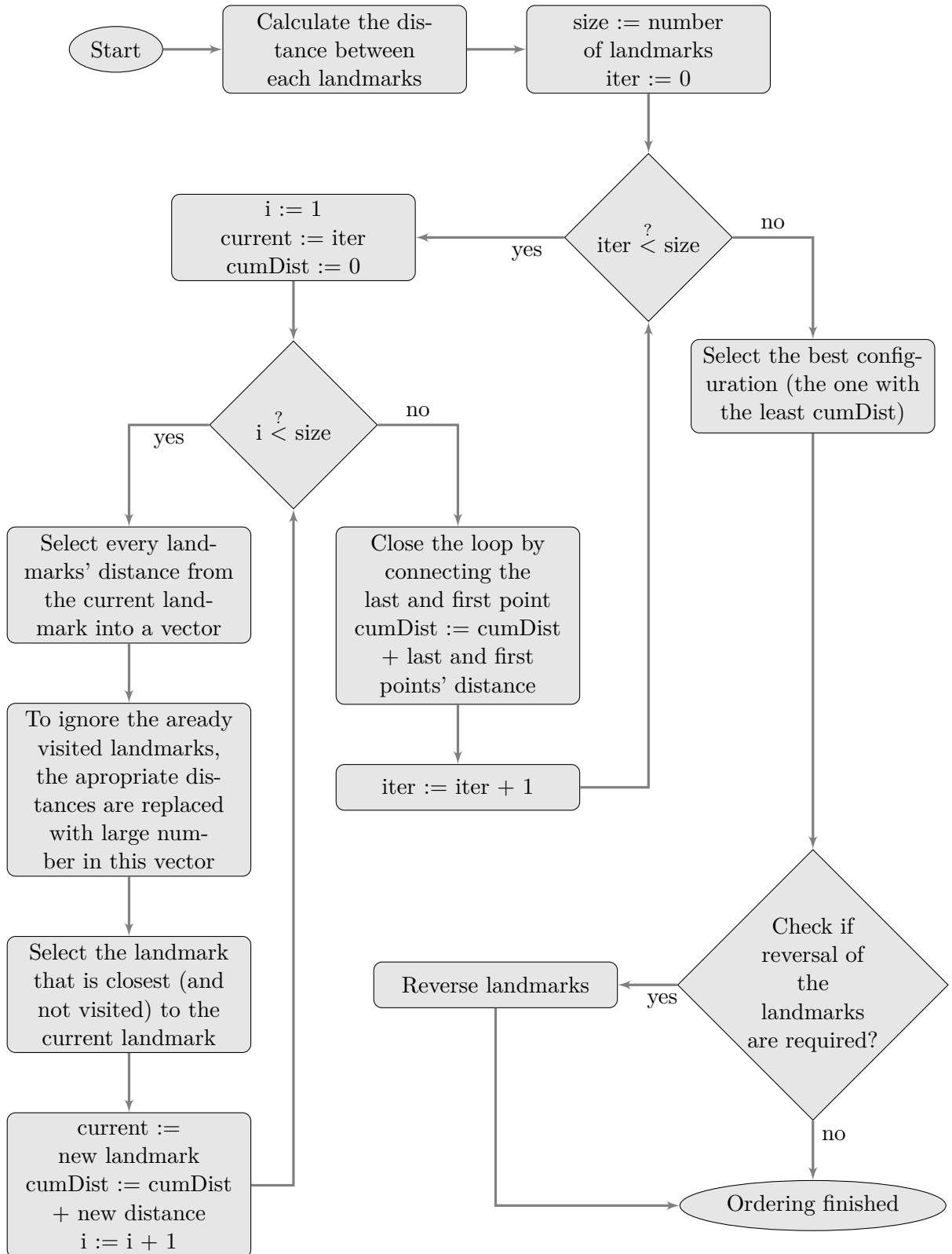


Figure 4.5: Landmark ordering method

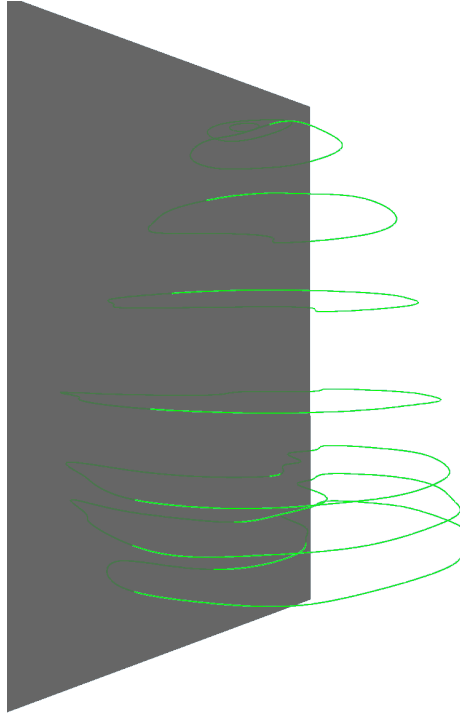


Figure 4.6: Plane rotation along the axis

4.2.3 Sorting and synchronisation of the layers (5th step)

To connect the different layers with Catmull-Rom spline it is necessary to properly order them. The order of the planes in the manual processing part can be arbitrary. This allows a later refinement of the model by inserting a layer where necessary.

In the initializing step, each layer's centre is calculated and inserted into a matrix:

$$points = \begin{bmatrix} x_0 & y_0 & z_0 \\ x_1 & y_1 & z_1 \\ & \vdots & \\ x_n & y_n & z_n \end{bmatrix} \quad (4.1)$$

Then a mean value is calculated which is the centre of the aforementioned centre points. A centring of the points in the matrix is achieved by subtracting this value from each row of the matrix:

$$\begin{aligned} c_x &= \frac{1}{n} \sum x_0 + x_1 + \dots + x_n \\ c_y &= \frac{1}{n} \sum y_0 + y_1 + \dots + y_n \\ c_z &= \frac{1}{n} \sum z_0 + z_1 + \dots + z_n \end{aligned} \quad (4.2)$$

An SVD (described in details in Section 3.7) is calculated for the coming processing methods:

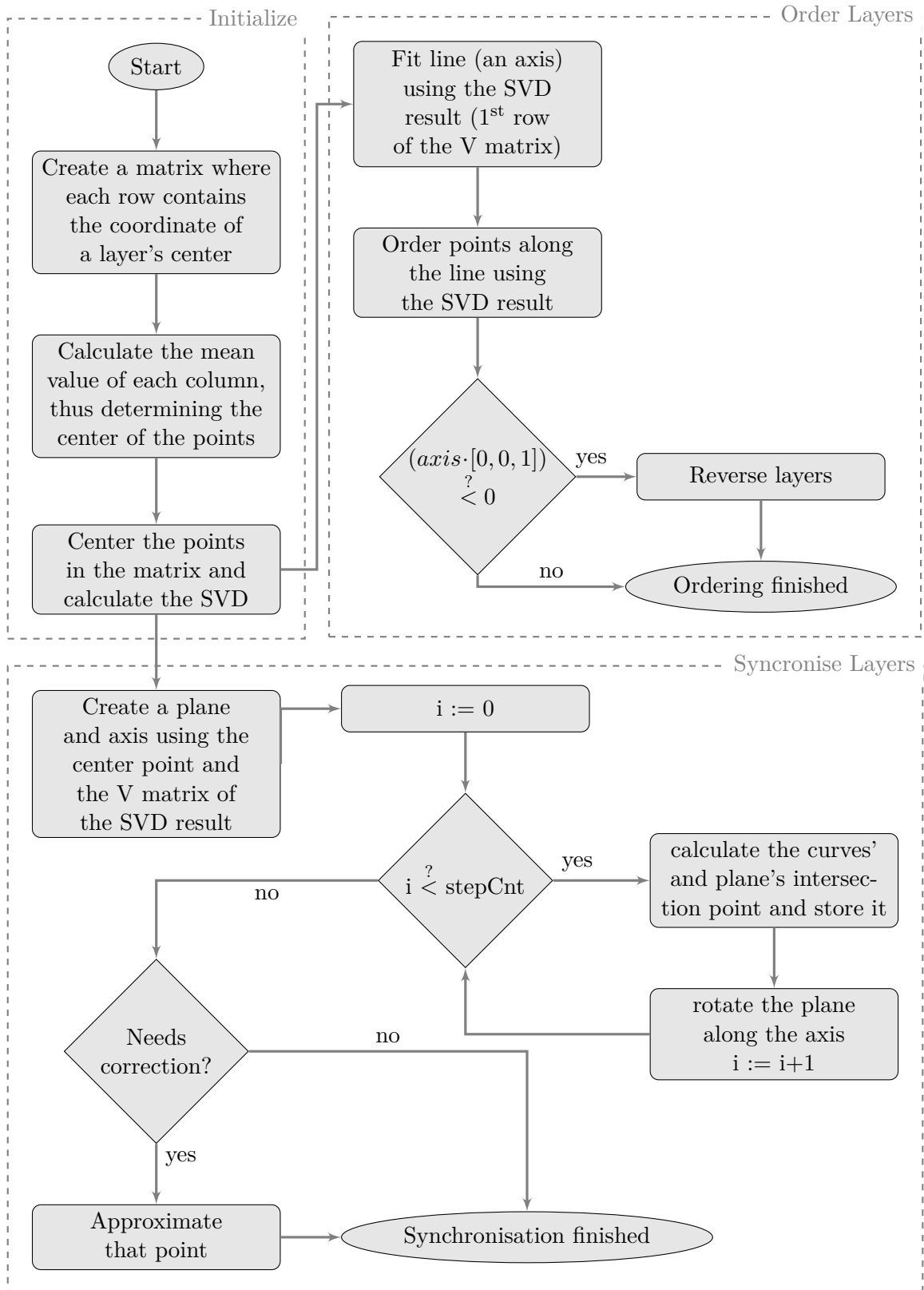


Figure 4.7: Layer sorting and synchronisation algorithm

$$centered\ points = \begin{bmatrix} c_{x0} & c_{y0} & c_{z0} \\ c_{x1} & c_{y1} & c_{z1} \\ \vdots & \vdots & \vdots \\ c_{xn} & c_{yn} & c_{zn} \end{bmatrix} = \begin{bmatrix} x_0 & y_0 & z_0 \\ x_1 & y_1 & z_1 \\ \vdots & \vdots & \vdots \\ x_n & y_n & z_n \end{bmatrix} - \begin{bmatrix} c_x & c_y & c_z \\ c_x & c_y & c_z \\ \vdots & \vdots & \vdots \\ c_x & c_y & c_z \end{bmatrix} \quad (4.3)$$

The above algorithm is summarized in Fig. 4.7.

'Order Layers' section of the Fig. 4.7 presents the main segment of the ordering algorithm. The centre of the layers are located around a line. A line is fitted on these points using the SVD result. The first row of the SVD resulted V matrix provides the vector for the line, while the mean value of each centre points gives a point on the line. Following the line fitting the ordering is done along this line using the SVD result. In the final step the direction of the ordering has to be checked to create a consistent result. This is done by calculating the dot product of the line's vector and $(0, 0, 1)$ vector. If the result is lower than zero the order of the layers are reversed.

To properly connect the adjacent layers with Catmull-Rom spline the B-spline curves has to be aligned. This is achieved by identifying the corresponding points – i.e. the points "below" each other – on the B-splines and synchronising them.

Fig. 4.7 presents this algorithm labelled as 'Synchronise Layers'. The synchronisation is done by slicing the curves with planes and calculating the intersection point with that plane. In the initializing step the plane is defined by the centre point calculated in the 'Initialize' step and a normal vector provided by the 2nd row of the SVD result's V matrix (presented in Fig. 4.6). Intersection points are calculated between this plane and all B-splines taking into account the direction of the B-spline curves. This means the normal vector of the plane has to have the same direction as the curve in order to consider the intersection point as a valid point. If multiple intersection points meet these criteria on any given B-spline the entire configuration is rejected. In the next step the plane is rotated with a predefined step along the axis given by the line introduced above in this section. In the new position of the plane the same calculations are done. This process is repeated until the plane makes a whole turn. In the finishing step the results are analysed and a linear approximation is applied for the invalid configurations as well as for plane positions where no intersection points exists to get an approximation for those.

4.2.4 Catmull-Rom spline fitting and preliminary mesh calculation (6th step)

The Catmull-Rom spline (introduced in Section 3.2) fitting process is described in Fig. 4.9. At first using the synchronisation markers introduced in Section 4.2.3 the B-splines are sampled. Predefined number of equally spaced sampling points are generated between each two synchronisation markers as shown on the left side of Fig. 4.8. These points are used as control points for the Catmull-Rom spline.

In the following step extra points are added before the first layer and after the last layer. It is required for the Catmull-Rom spline fitting, since this spline is only drawn between the second and the penultimate control point. The corresponding points are connected. This intermediate result is demonstrated on the right side of Fig. 4.8. Finally a Catmull-Rom spline is fitted using these control points.

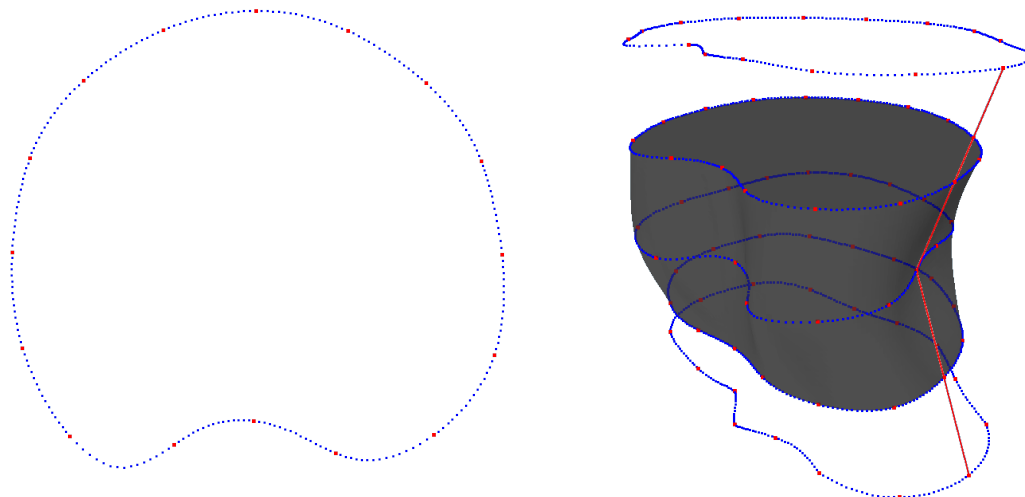


Figure 4.8: Left: Sampling points on the B-spline. Red: Synchronisation markers, Blue: Sampling points
 Right: Sampling points on a vertebral body model for Catmull-Rom spline fitting

To generate a mesh for visualization the Catmull-Rom splines have to be sampled. The sampling is achieved by intersecting the splines with predetermined planes. A plane is fitted on all B-splines, then using linear approximation intermediate planes are generated. The intersection point between each generated planes and each Catmull-Rom spline are evaluated using the well-known bisection method. These intersection points are the elements of the preliminary mesh.

4.2.5 Triangulation (7th step)

The surface visualization is achieved by triangulating the model. This process is done by using the preliminary mesh, in two main phases:

1. Plate mesh: The terminating - i.e. top and bottom - plate of the model, e.g. the vertebral body's base plate.
2. Surface mesh: The surface between the terminating plates of the model.

4.2.5.1 Plate mesh

The plate triangulation algorithm is presented in Fig. 4.10. Depending on the building block (see Section 4.1.1) used on the current layer two scenarios are distinguished. When the curve on the layer is simple the triangulation of the enclosed area can be done without any additional steps (see left image in Fig. 4.11). In any other cases when an organ with cavity (or concave shape) is being modelled the closing cap of this cavity is triangulated in the same way using the internal curve of the layer (see middle image in Fig. 4.11). When neither of the conditions are true some additional processing steps are required. The intersection points are calculated between the two curves (outer and inner) and these points are added to the triangulation. Segments of the curves are jettisoned where the inner curve runs outside the polygon determined by the outer curve. After these steps the triangulation is executed (see right image in Fig. 4.11).

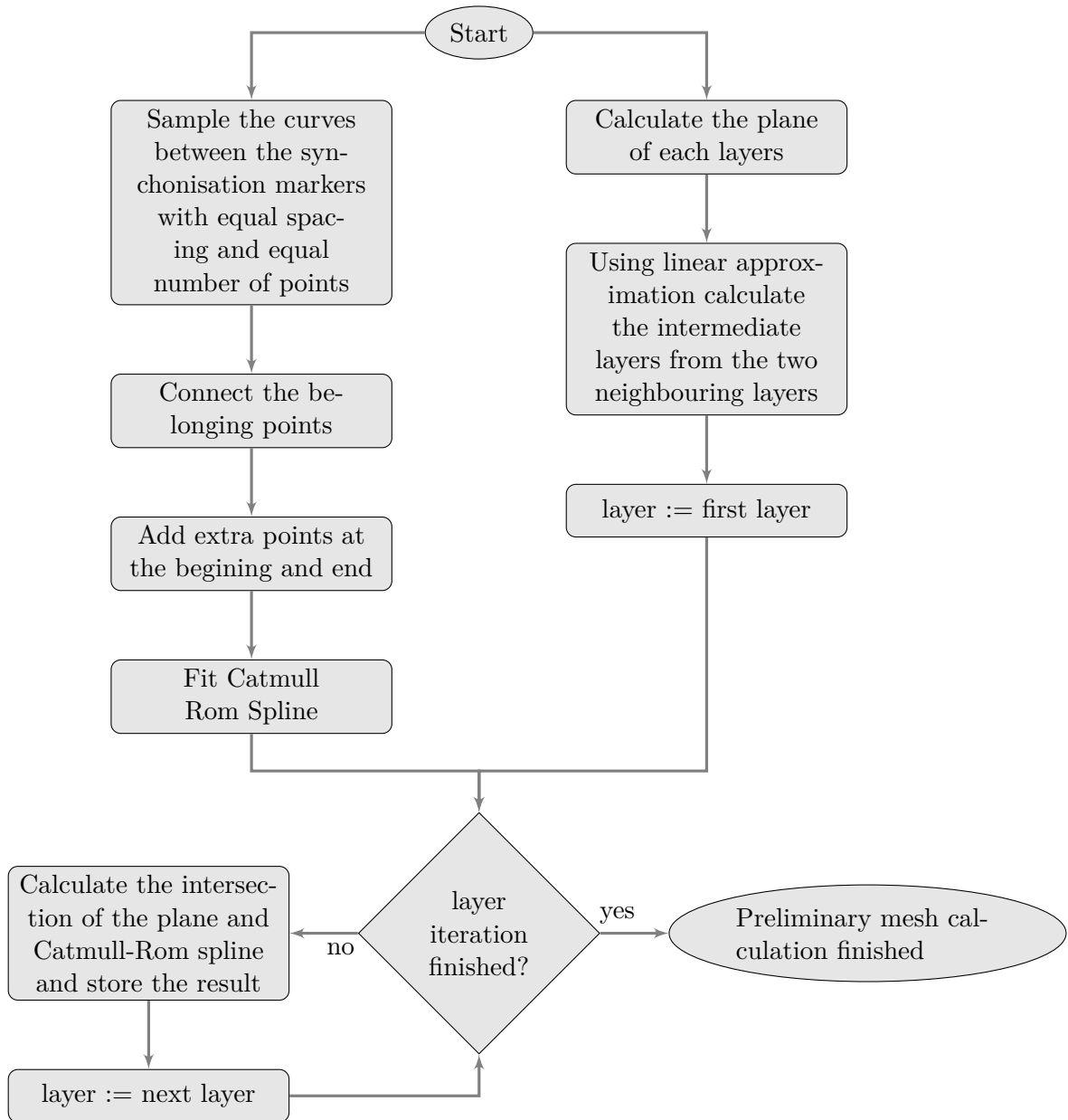


Figure 4.9: Catmull-Rom spline fitting and calculation algorithm of the preliminary mesh

4.2.5.2 Surface mesh

The surface mesh generation process is introduced in Fig. 4.12. When any adjacent curve is simple (as introduced in Section 4.1.1) the preliminary mesh can be used directly as a triangular mesh by slicing each quadrilaterals into triangles. When both adjacent curves are non-simple a more sophisticated algorithm is required to properly triangulate the side of the model. The initial steps are the same as presented in Section 4.2.5.1. Following that a triangulation of two neighbouring layers interposed over each other in a 2 dimensional space is done. Look up of the original coordinates is necessary in order to convert back the result into 3D space. The intersection points' position is also calculated in the 3

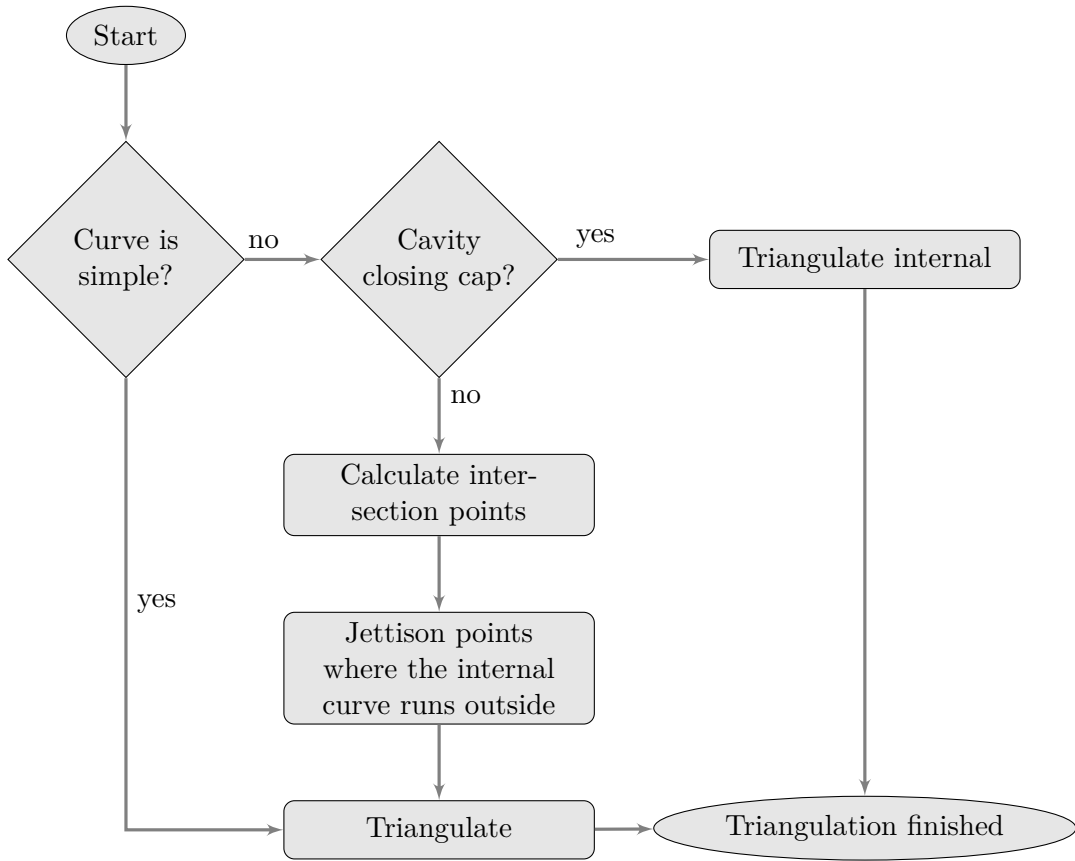


Figure 4.10: Plate triangulation method

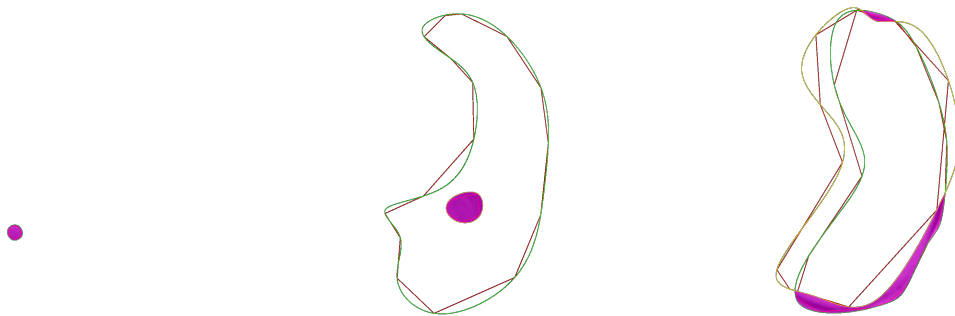


Figure 4.11: Plane triangulation examples; the purple area is being triangulated; green curve: outer border, yellow curve: inner border. Left: Simple curve; Middle: Internal part is triangulated; Right: Complex triangulation

dimensional coordinate system. In the finishing step extra triangles are added based on these intersection points.

A vertebral body's triangulated model is presented in Fig. 4.13.

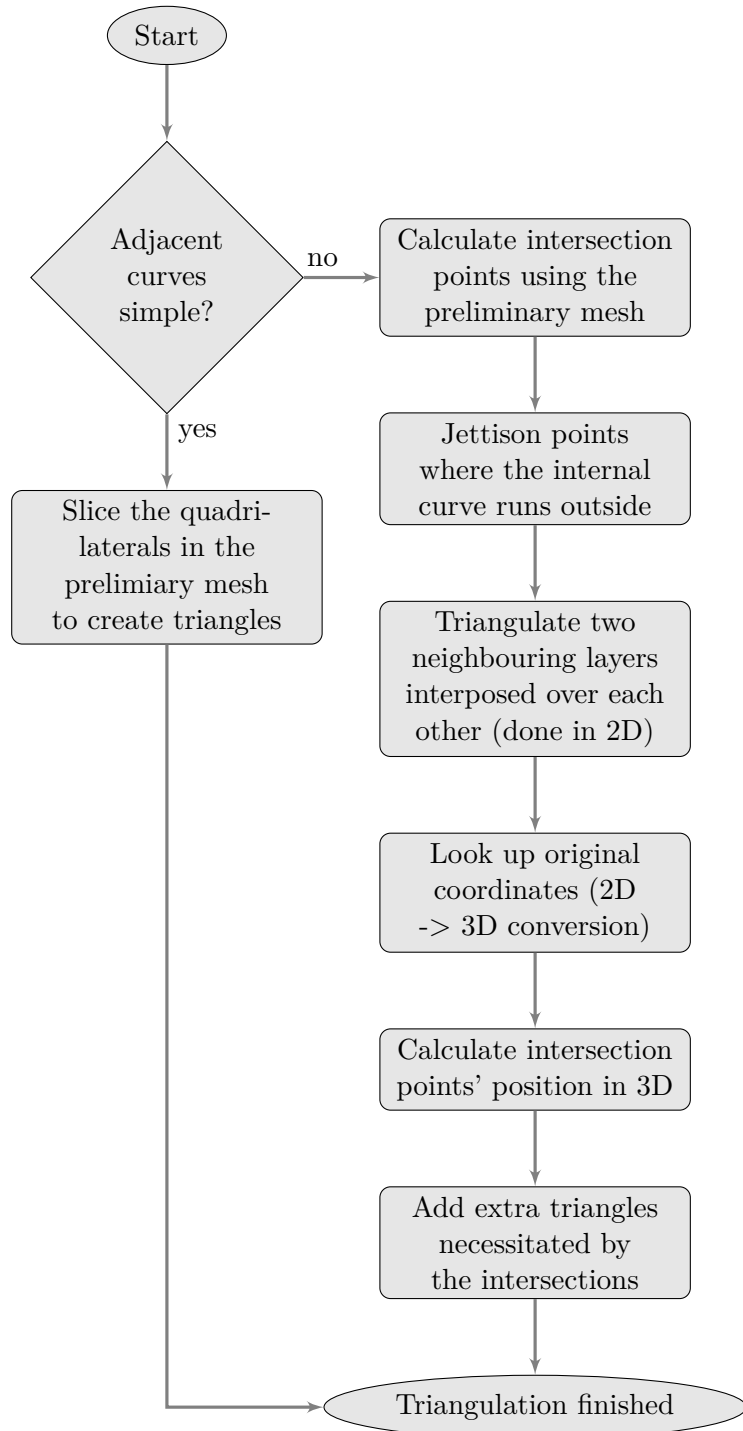


Figure 4.12: Surface triangulation algorithm

4.3 Comparison

Four patients' lumbar section of the spinal column were modelled to validate our model. This means in total 20 vertebral bodies were analysed. The reference mask were obtained along with the database of the medical images. Following the validation process (introduced in Section 3.10) we evaluated Hausdorff distance and Dice coefficient (Section 3.9) to quantitatively measure the precision of the geometrical model along with the entire model

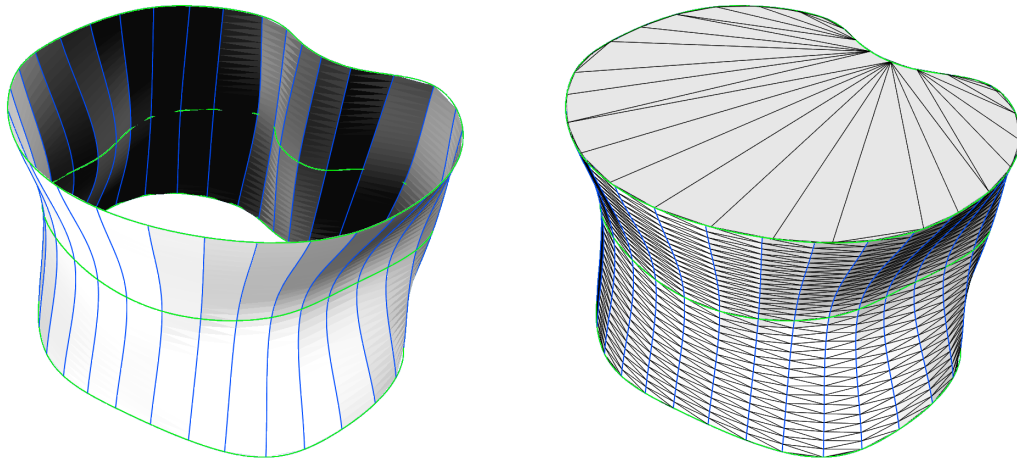


Figure 4.13: Surface of the geometrical model (vertebral body model)

Subject	Vertebra	Max [mm]	Avg [mm]	95% [mm]
Subject01	L1	3.33	0.47	1.09
Subject01	L2	4.51	0.66	2.14
Subject01	L3	4.11	0.55	1.55
Subject01	L4	4.28	0.95	2.74
Subject01	L5	12.27	0.96	2.96
Subject06	L1	2.88	0.44	1.53
Subject06	L2	3.29	0.62	2.39
Subject06	L3	4.39	0.85	1.53
Subject06	L4	3.48	0.89	2.68
Subject06	L5	8.23	0.75	1.84
Subject08	L1	4.01	0.87	2.72
Subject08	L2	4.58	0.86	2.60
Subject08	L3	4.98	1.06	3.02
Subject08	L4	3.09	0.85	2.01
Subject08	L5	3.72	0.83	2.03
Subject10	L1	5.15	0.69	1.70
Subject10	L2	6.40	0.91	2.24
Subject10	L3	3.54	0.89	2.18
Subject10	L4	4.33	1.12	2.61
Subject10	L5	9.47	1.50	4.02
Average		5.00	0.84	2.28
Standard deviation		2.39	0.24	0.67

Table 4.1: Vertebral body model comparison with reference using Hausdorff metric

fitting process. The achieved Hausdorff distance metrics are summarized in Table 4.1 and the Dice coefficient results in Table 4.2.

The model were validated on another database containing CT images of lungs. 5 patients' medical image were processed, meaning 10 lungs were analysed, using the workflow introduced in this chapter. The database were provided with a reference segmentation, which

Subject	Vertebra	Dice coeff [%]	True pos+neg [%]	False pos [%]	False neg [%]
Subject01	L1	95.21	95.55	1.42	3.03
Subject01	L2	93.50	93.92	3.16	2.92
Subject01	L3	94.64	94.30	1.88	3.82
Subject01	L4	92.56	92.27	1.54	6.19
Subject01	L5	91.62	93.42	1.04	5.54
Subject06	L1	94.32	95.25	1.18	3.56
Subject06	L2	93.30	94.00	2.54	3.46
Subject06	L3	92.38	92.77	3.93	3.30
Subject06	L4	91.69	92.84	1.59	5.57
Subject06	L5	91.21	94.61	2.36	3.03
Subject08	L1	92.45	93.88	1.21	4.92
Subject08	L2	92.60	93.66	1.58	4.76
Subject08	L3	91.26	91.27	1.58	7.15
Subject08	L4	92.89	92.66	1.55	5.79
Subject08	L5	92.03	95.59	0.76	3.65
Subject10	L1	92.55	95.05	2.09	2.86
Subject10	L2	90.38	93.16	1.90	4.94
Subject10	L3	90.79	92.25	1.87	5.88
Subject10	L4	88.22	89.83	1.16	9.01
Subject10	L5	83.35	92.03	1.03	6.94
Average		91.85			
Standard deviation		2.54			

Table 4.2: Vertebral body model comparison with reference using Dice metric

Lung	Avg [<i>mm</i>]	95% [<i>mm</i>]
S1-101_Left	2.60	9.21
S1-101_Right	3.17	11.37
S1-102_Left	3.43	9.69
S1-201_Left	2.25	6.23
S1-201_Right	3.30	10.92
S2-101_Left	3.06	10.86
S2-101_Right	3.18	10.22
S2-102_Left	2.59	7.01
S2-102_Right	3.22	10.23
Average	2.97	0.40
Standard deviation	9.53	1.78

Table 4.3: Lung model comparison with reference using Hausdorff metric

were used in the validation process. The Hausdorff distance and Dice coefficient of the comparison are detailed in Table 4.3 and 4.4.

Finally the achieved Dice coefficients of the two models are compared in Fig. 4.14.

Lung	Dice coeff [%]	True pos+neg [%]	False pos [%]	False neg [%]
S1-101_Left	94.37	97.71	1.64	0.65
S1-101_Right	94.42	97.46	1.49	1.05
S1-102_Left	94.12	98.14	1.17	0.70
S1-102_Right	93.72	97.79	1.45	0.76
S1-201_Left	93.17	97.58	1.39	1.02
S1-201_Right	92.94	97.26	1.88	0.86
S2-101_Left	91.70	96.63	1.87	1.50
S2-101_Right	91.98	96.87	1.83	1.30
S2-102_Left	94.20	97.57	1.14	1.29
S2-102_Right	93.21	97.33	1.51	1.16
Average	93.38			
Standard deviation	0.97			

Table 4.4: Vertebral body model comparison with reference using Dice metric

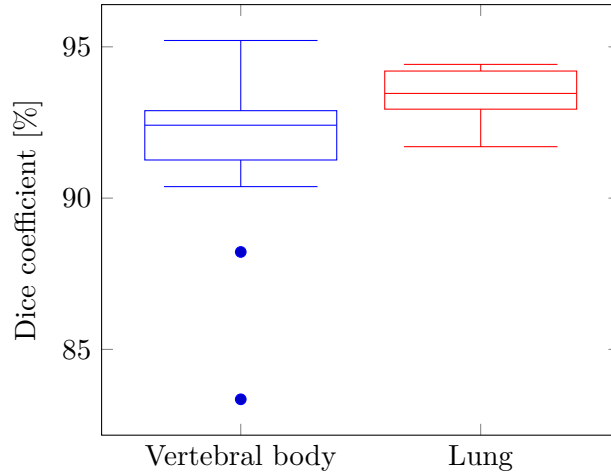


Figure 4.14: Box plot of the Dice coefficients

4.4 Diagnostic parameters

This paper’s goal is not to provide a detailed description of diagnostic parameter calculation, rather to present the geometrical model along with a brief introduction into the calculation of clinically relevant parameters of the given organ. Two important diagnostic parameter evaluations are presented here:

1. Angle measurement for spinal column diagnostics;
2. Multi purpose volume calculation.

4.4.1 Angle measurement

The automatic angle measurement for the spinal column model were discussed in our previous article [27]. In the diagnostic of the spinal column several angles are used to evaluate the condition of the patient’s health and decide the best treatment. The manual measurement process of these angles are time consuming, prone to error and suffer from

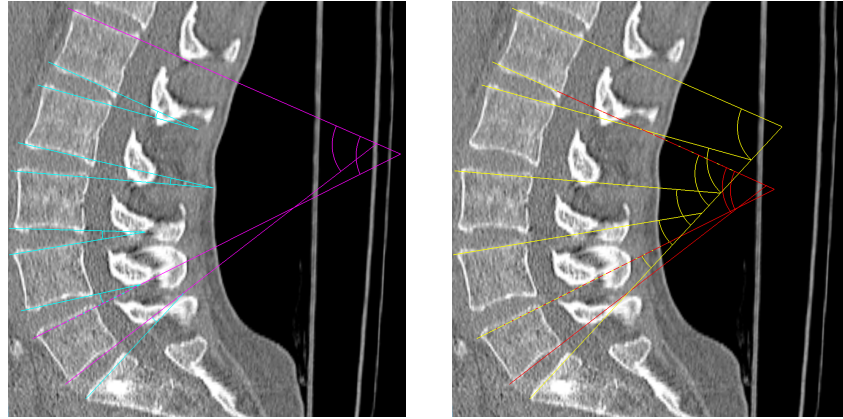


Figure 4.15: Measured angles on the lumbar section of the spinal column

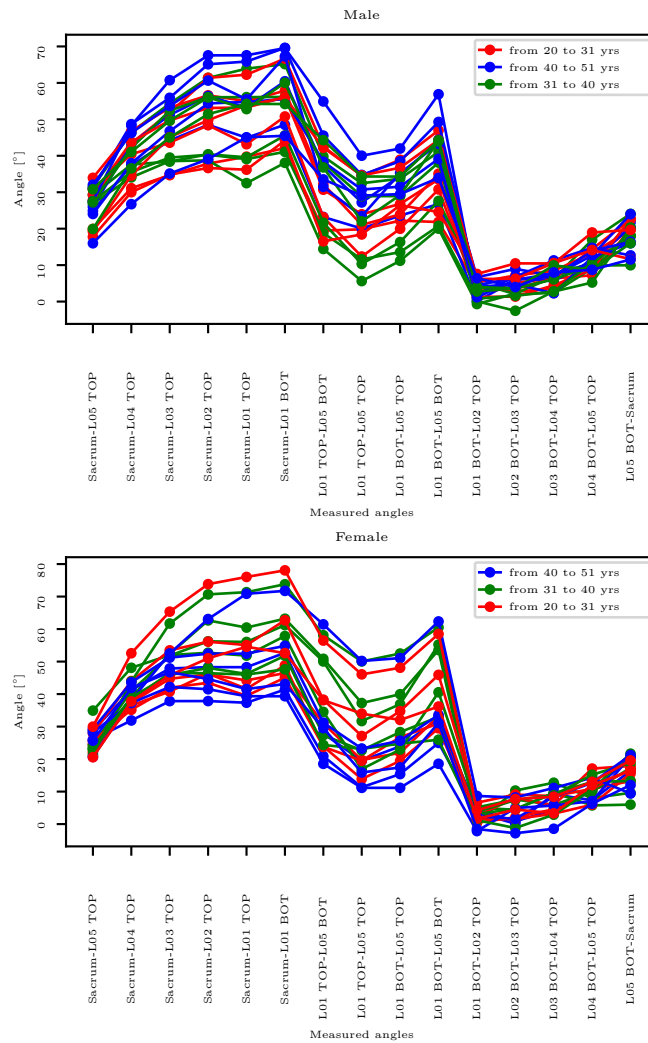


Figure 4.16: Measured diagnostic parameters (spinal column angles) of 39 patients that are commonly used in orthopaedic practice

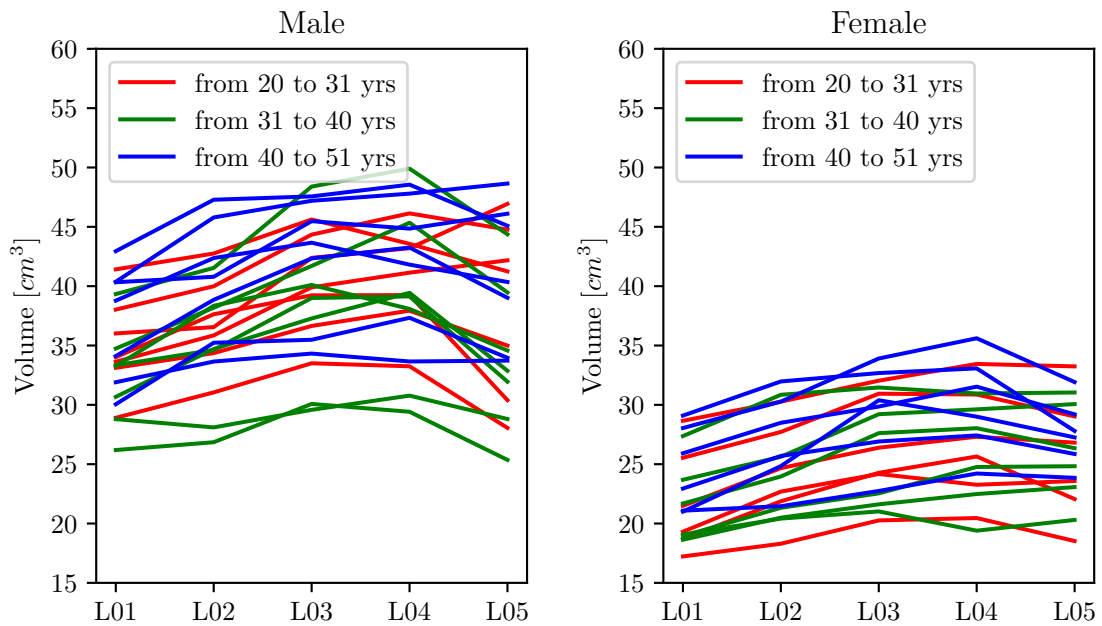


Figure 4.17: Measured diagnostic parameters (vertebral body volumes) of 39 patients

poor reproducibility. These issues can be mitigated to some degree by using the presented geometrical model.

The angle measurement in the clinical practice is done in the central sagittal plane. To automatically measure angle this plane had to be identified in the initial step. We achieved this by finding the best fitting symmetry plane for the spinal column’s geometrical model. In the next step the angles are measured in this plane using the base plate of the individual vertebrae. Automatically generated measurement angles on the lumbar section of the spinal column are shown in Fig. 4.15.

Another application for the model based angle measurement can be found in the field of clinical studies, where the reproducibility is a key expectation. This is demonstrated in Fig. 4.16 where 39 patients lumbar section of the spinal column were analysed.

4.4.2 Volume calculation

With a traditional medical image visualization systems it is often difficult and time consuming or unfeasible to calculate the volume of a given organ. However, sometimes this information could be beneficial for the diagnostic and therapy of various conditions. The proposed geometrical model allows easy and fast determination of the given organ’s volume. A brief example for this application is presented in Fig. 4.17.

Chapter 5

Discussion

5.1 Automatic fitting algorithms

This part of the paper provides a short overview of the automatic processing steps introduced in Section 4.2 along with their strength and limitations.

5.1.1 Sorting the marked anatomical points

The anatomical marker sorting algorithm provides excellent results in almost all the modelling cases; it is exceptionally robust in modelling convex shapes. However, when the anatomical structure has a sharp edge, and the shape is extremely concave, the marker sorting algorithm may suggest an undesired order of the marked anatomical points. As an example for this extreme case, see the left part of Fig. 5.1 where the corner landmark is isolated. However, the major benefit of the proposed algorithm is that this modelling mistake can be intuitively corrected by adding additional landmarks, as it is shown on the right side of Fig. 5.1. The algorithm is designed so that the undesired marker ordering

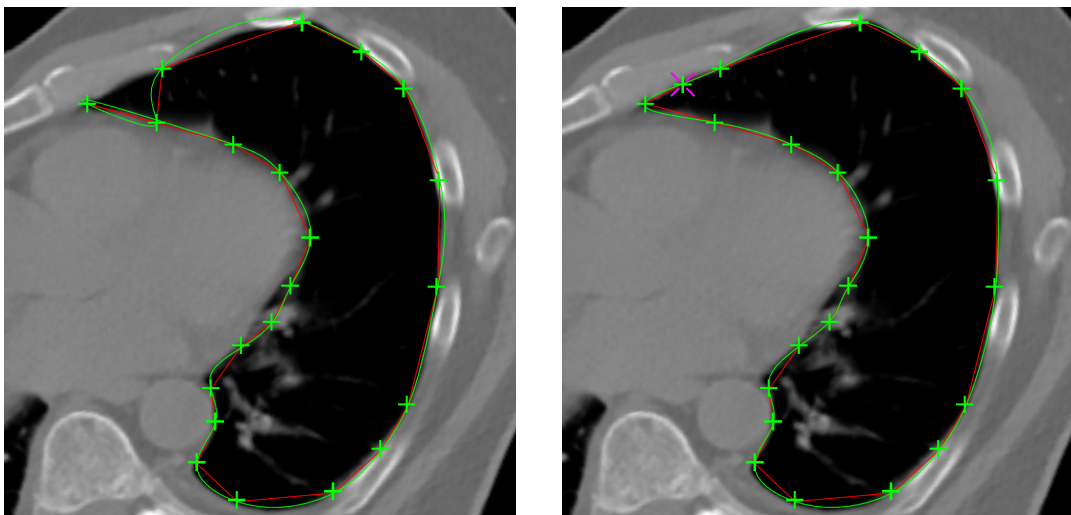


Figure 5.1: Error caused by the isolation of the corner landmark. Left: an incorrect configuration; Right: corrected ordering

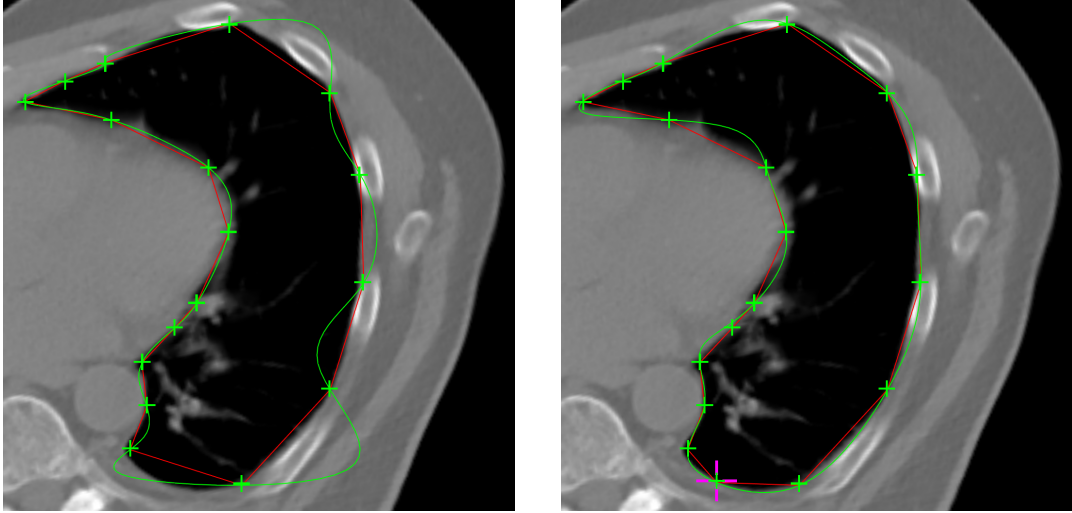


Figure 5.2: B-spline fitting wavy curve. Left: configuration with issue; Right: corrected curve

can be easily recognized. The additional marker will automatically correct the order of the landmarks as shown on the right side of the figure.

5.1.2 B-spline fitting

The greatest challenge in the B-spline fitting process is finding the ideal number of control points for the spline. Selecting too few points means the curve would be unable to follow the complex shape of the anatomical structure. On the other hand, too many points cause the curve to wiggle. Thus, the modelling building blocs using B-splines are implemented so that the number of control points can be set for each use of the building block. This way, the number of control points is individually defined for each organ model.

Thanks to this flexibility, in most configurations, the spline approximates the landmarks in the expected way. In some rare cases when the result would be unacceptably wavy, e.g., in the case shown on the left side of Fig. 5.2, the curve can be fixed again intuitively by adding additional landmark point (see right side of Fig. 5.2).

5.1.3 Sorting and synchronisation of the layers

The sorting algorithm worked appropriately in our experiments. The synchronisation workflow produces almost always the desired result. However, due to its simple construction it has some limitations, the most notable one when the model has a corner segment in multiple layers. In this scenario, it is possible to wrap the surface around this corner creating an unwanted warp in the surface (shows in Fig. 5.3). The synchronisation algorithm incorrectly connects two points on the opposite side of the corner as the corresponding point, thus causing the warp. A possible solution would be the implementation of a more robust algorithm that can identify these key points and appropriately handle them. This improvement will be a subject of further work.

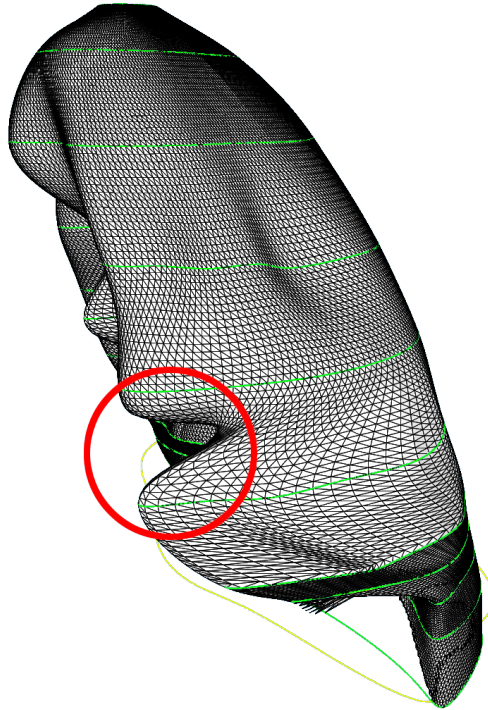


Figure 5.3: Layer synchronisation limitation in a special case

5.1.4 Triangulation

The triangulation algorithm works perfectly when the terminating plates are processed. It also operates without any issue on the side surface of the model as long as only simple curves are used. However, when two splines are utilized in a single layer, the limitation of the algorithm can be seen in the form of missing triangles. An example of this behaviour is presented in Fig. 5.4. The algorithm used here triangulates in a 2D space, then a 3D mapping of the vertices creates a 3D triangulation from the 2D result. This means the

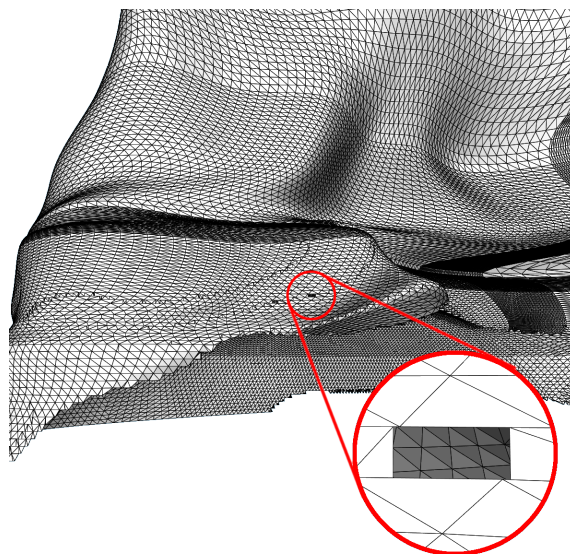


Figure 5.4: Limitation of the triangulation algorithm

lack of depth sensing in the algorithm that causes issues when two edges in the polygons representing the B-spline curves are positioned on top of each other.

5.1.5 Achieved precision of the model

This modelling approach enables the precise manual segmentation of different organs. On the validation dataset of 20 vertebral bodies the Dice coefficient reached an average of $91.9 \pm 2.54\%$ and the Hausdorff metric achieved $2.28 \pm 0.67 \text{ mm}$ on the 95%. The other database, containing 10 lungs, achieved similar accuracy, when comparing the reference segmentation with our model the Dice coefficient reached $93.4 \pm 0.97\%$. These errors are in the acceptable range for medical diagnostics purposes, meaning the model is suitable for that purpose.

The diagnostics parameters, as demonstrated in Section 4.4, can be easily and automatically calculated given the geometrical model of the organ is available. That means the time consuming determination process of complex or large number of diagnostics parameters can be done within seconds by automatically calculating these values. This clinical parameter determination process is only feasible when the manual model fitting task does not require too much time. Our measurements show that a typical vertebral body can be fully modelled under 5 minutes, while the more complex lung requires around 30 minutes. The latter could be improved by more carefully analysing the modelling layers' placement (the first step in Fig. 4.2), thus reducing the necessary number of layers.

We demonstrated the model's applicability on vertebral bodies and lungs. The Dice coefficient when comparing the results with a reference segmentation were in the same range ($91.9 \pm 2.54\%$ for the vertebral body and $93.4 \pm 0.97\%$ for the lung). Thus, the geometrical model presented in this paper can be considered robust for various modelling and segmen-

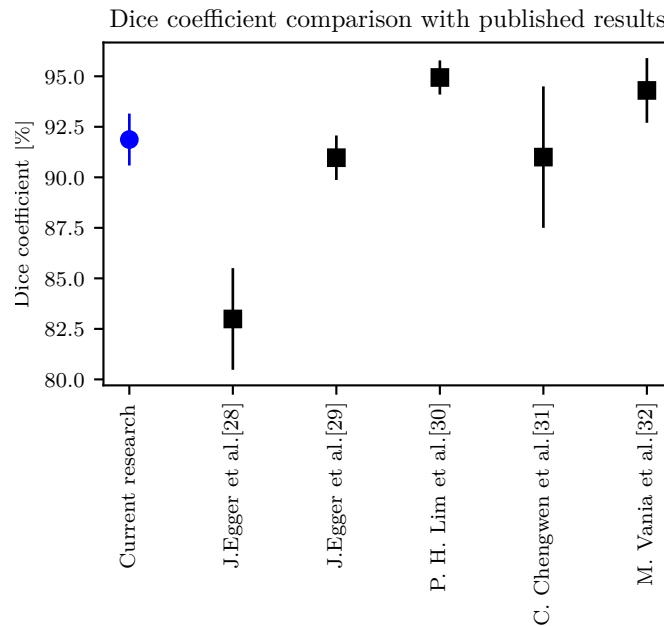


Figure 5.5: Dice coefficient comparison with results published by other authors (vertebral body)

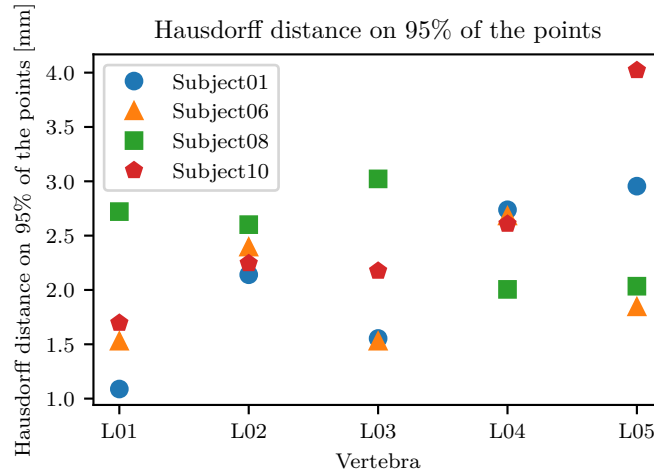


Figure 5.6: Hausdorff distance on 95% of the points (vertebral body)

tation tasks in the medical field. The model is suitable for analysing complex anatomical structures (such as lung), as well as organs with simple shapes (e.g. vertebral body) too.

The precision of the model is considered to be very accurate compared to results published in papers dealing with similar problems. Fig. 5.5 shows the achieved Dice coefficient with the vertebral body model along with publication in this field, however, those results cannot be directly compared with this research, since our goal was to provide an easy to use geometrical model which can be defined by limited number of markers. On the other hand most of the paper's goal in this field is to model as precisely as possible the organ. Based on this results we can conclude that using our model does not introduce larger errors, than using the ones available in these papers. Fig. 5.6 shows the achieved Hausdorff distance with the vertebral body model when the worst 5% of the points is discarded.

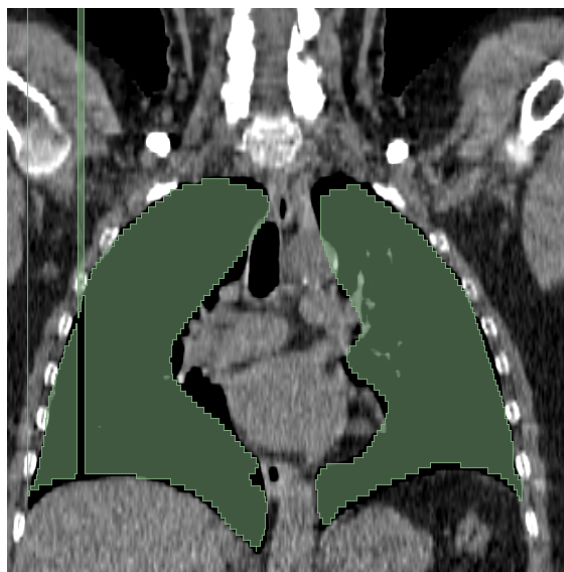


Figure 5.7: Artefacts on the voxelized lung model

We were unable to evaluate a meaningful Hausdorff metric for the lung model, due to the limitation of the triangulation algorithm (this limitation is presented in Section 5.1.4). The missing triangles caused issues in the voxelization process of the triangular mesh, which is a necessary step before the Hausdorff metric calculation. For this reason the resulted voxelized model had artefacts in form of unwanted rays at the superior side of the lung (illustrated in Fig. 5.7). This limitation of the model also introduces error in the Dice coefficient, since the evaluation of this metric also require voxelization, but the volume of these artefacts negligible compared to the entire lung, thus, not effecting the result significantly. In contrast, the Hausdorff metric is constructed specifically to detect this kind of deviations, therefore being inapplicable in this scenario.

Chapter 6

Conclusions

In the presented research, the building blocks for geometric modelling are defined making it possible to create multiple different organ models with associated optimisation steps. The organ models defined by the proposed modelling approach enable rapid segmentation of organs and automatic creation of medical diagnostic parameters.

Two concrete organ models, a vertebral body model and a lung model, have been developed and used to validate the proposed modelling approach. The created organ models use the same building blocks. The resulting geometric models were validated and analysed from different aspects to validate their eligibility for the calculation of diagnostic parameters.

This modelling approach and diagnostic parameter identification methods were implemented in an integrated environment, making it possible for medical experts to use these methods directly. Many optimization steps were introduced in this environment to accelerate the image segmentation and diagnostic parameter definition process and improve the user experience. The proposed models and associated diagnostic framework enable large-scale medical studies by segmenting dozens or hundreds of patient images and creating diagnostic databases.



Figure 6.1: The modelling framework

6.1 Further work

Since reusable building blocks were designed, in the future, more human organs can be modelled using them for both diagnostic and simulation purposes. Potentially, a domain-specific language (DSL) could be implemented for simplified model building using abstract descriptions, which could further accelerate the modelling process.

Acknowledgements

The authors would like to express their gratitude to Dr. Tamás Umenhoffer for helping them to setup the modelling framework, assisting and giving advices for it's usage. We are grateful for Prof. Tamás László Várady and Dr. Péter Salvi for their help in the designing the first version of the model. We would like to thank Diána Kőrösi and Dóra Kapui for their help in the modelling.

Bibliography

- [1] Illustration of the trachea and lung lobes. illustration by mayank mehrotra. <https://www.ncbi.nlm.nih.gov/books/NBK532952/figure/article-31159.image.f1/>. Accessed: 2021-10-27.
- [2] Cc by 4.0 licence. <https://creativecommons.org/licenses/by/4.0/>. Accessed: 2021-10-27.
- [3] Naoki Kamiya. Muscle segmentation for orthopedic interventions. *Intelligent Orthopaedics. Advances in Experimental Medicine and Biology*, 1093, 2018.
- [4] Pedro P. Rebouças Filho, Paulo Cesar Cortez, and Victor Hugo C. de Albuquerque. 3d segmentation and visualization of lung and its structures using ct images of the thorax. *J. Biomedical Science and Engine*, 2013.
- [5] Lauren Lauren Jean O'Donnell. *Semi-automatic medical image segmentation*. PhD thesis, Massachusetts Institute of Technology, 2001.
- [6] Eli Gibson, Francesco Giganti, Yipeng Hu, Ester Bonmati, Steve Bandula, Kurinchi Gurusamy, Brian Davidson, Stephen P Pereira, Matthew J Clarkson, and Dean C Barratt. Automatic multi-organ segmentation on abdominal ct with dense v-networks. *IEEE transactions on medical imaging*, 37(8):1822–1834, 2018.
- [7] Juying Huang, Fengzeng Jian, Hao Wu, and Haiyun Li. An improved level set method for vertebra ct image segmentation. *Biomedical engineering online*, 12(1):1–16, 2013.
- [8] D. Müller and F. Kramer. Miscnn: a framework for medical image segmentation with convolutional neural networks and deep learning. *BMC Med Imaging*, 2021.
- [9] Mhd Saeed Sharif, Maysam Abbod, Abbes Amira, and Habib Zaidi. Artificial neural network-based system for pet volume segmentation. *International journal of biomedical imaging*, 2010, 2010.
- [10] H. Lee, F.M. Troschel, S. Tajmir, G. Fuchs, J. Mario, F.J. Fintelmann, and S. Do. Pixel-level deep segmentation: Artificial intelligence quantifies muscle on computed tomography for body morphometric analysis. *J Digit Imaging*, 30:487–498, 2017.
- [11] Yang Lei, Yabo Fu, Tonghe Wang, Richard L.J. Qiu, Walter J. Curran, Tian Liu, and Xiaofeng Yang. Deep learning in multi-organ segmentation. 2020.
- [12] Nicola Cappetti, Alessandro Naddeo, Arcangelo Pellegrino, Giovanni Francesco Solitro, and Francesco Naddeo. Parametric model of lumbar vertebra. *J. Ind. Des. Eng. Graph*, 7:515–518, 2010.
- [13] Nikola Vitković, Jelena Mitić, Miodrag Manić, Miroslav Trajanović, Karim Husain, Slađana Petrović, and Stojanka Arsić. The parametric model of the human mandible

- coronoid process created by method of anatomical features. *Computational and Mathematical Methods in Medicine*, 2015, 2015.
- [14] Darko Štern, Boštjan Likar, Franjo Pernuš, and Tomaž Vrtovec. Parametric modelling and segmentation of vertebral bodies in 3d CT and MR spine images. 56(23):7505–7522, nov 2011.
- [15] Sandor Bazso. Geometric modelling of the human vertebral body for diagnostics purposes. *BME-VIK Scientific Students' Association Report*, 11 2020.
- [16] Sándor Bazsó, Árpád Viola, and Balázs István Benyó. Personalisable vertebral body model development. In *2021 IEEE 25th International Conference on Intelligent Engineering Systems (INES)*, pages 000127–000132, 2021.
- [17] Szirmay-Kalos Laszlo, Gyorgy Antal, and Ferenc Csonka. *Haromdimenzios grafika, animacio es jatekfejlesztes*. ComputerBooks, Budapest, Hungary, 2003.
- [18] Michael Felsberg, Per-Erik Forssén, and Hanno Schar. Channel smoothing: Efficient robust smoothing of low-level signal features. *IEEE transactions on pattern analysis and machine intelligence*, 28:209–22, 03 2006.
- [19] Cc by-sa 2.0 licence. <https://creativecommons.org/licenses/by-sa/2.0/>. Accessed: 2020-10-28.
- [20] Jorge Barbosa, Bruno Figueiredo, Nuno Bettencourt, and Joao Tavares. Towards automatic quantification of the epicardial fat in non-contrasted ct images. *Computer methods in biomechanics and biomedical engineering*, 14:905–14, 03 2011.
- [21] Bulat Ibragimov, Bostjan Likar, Franjo Pernus, and Tomaž Vrtovec. Shape representation for efficient landmark-based segmentation in 3-d. *Medical Imaging, IEEE Transactions on*, 33:861–874, 04 2014.
- [22] Robert Korez, Bulat Ibragimov, Bostjan Likar, Franjo Pernus, and Tomaž Vrtovec. A framework for automated spine and vertebrae interpolation-based detection and model-based segmentation. *IEEE transactions on medical imaging*, 34, 01 2015.
- [23] Website: Cancer image archive. <https://wiki.cancerimagingarchive.net/display/Public/Lung+CT+Segmentation+Challenge+2017#tui-tabs-responsive-trigger-0>. Accessed: 2021-10-27.
- [24] J. Yang, H. Veeraraghavan, S. G. Armato, K. Farahani, J. S. Kirby, J. Kalpathy-Kramer, W. van Elmpt, A. Dekker, X. Han, X. Feng, P. Aljabar, B. Oliveira, B. van der Heyden, L. Zamdborg, D. Lam, M. Gooding, and G. C. Sharp. Autosegmentation for thoracic radiation treatment planning: A grand challenge at AAPM 2017. *Med Phys*, 45(10):4568–4581, Oct 2018.
- [25] Kenneth Clark, Bruce Vendt, Kirk Smith, John Freymann, Justin Kirby, Paul Koppel, Stephen Moore, Stanley Phillips, David Maffitt, Michael Pringle, Lawrence Tarbox, and Fred Prior. The cancer imaging archive (tcia): Maintaining and operating a public information repository. *Journal of Digital Imaging*, 26(6):1045–1057, Dec 2013.
- [26] C. Pinter, A. Lasso, A. Wang, D. Jaffray, and G. Fichtinger. Slicerrt – radiation therapy research toolkit for 3d slicer. *Med. Phys.*, 39(10):6332–6338, 2012.
- [27] Sándor Bazsó, Árpád Viola, and Balázs István Benyó. Human spinal column diagnostic parameter identification using geometrical model of the vertebral body. In *2021 11th IFAC Symposium on Biological and Medical Systems*, 2021.

- [28] J. Egger, C. Nimsky, and X. Chen. Vertebral body segmentation with Grow-Cut: Initial experience, workflow and practical application. *SAGE Open Med*, 5:2050312117740984, 2017.
- [29] Jan Egger, Tina Kapur, Thomas Dukatz, Malgorzata Kolodziej, Dženan Zukić, Bernd Freisleben, and Christopher Nimsky. Square-cut: A segmentation algorithm on the basis of a rectangle shape. *PloS one*, 7:e31064, 02 2012.
- [30] P. H. Lim, U. Bagci, and L. Bai. Introducing willmore flow into level set segmentation of spinal vertebrae. *IEEE Transactions on Biomedical Engineering*, 60(1):115–122, 2013.
- [31] Chu Chengwen, Daniel Belavy, Gabi Armbrecht, Paul Bansmann, Dieter Felsenberg, and Guoyan Zheng. Fully automatic localization and segmentation of 3d vertebral bodies from ct/mr images via a learning-based method. *PLOS ONE*, 10:e0143327, 11 2015.
- [32] Malinda Vania, Dawit Mureja, and Deukhee Lee. Automatic spine segmentation from ct images using convolutional neural network via redundant generation of class labels. *Journal of Computational Design and Engineering*, 6(2):224 – 232, 2019.